BALABANOV, DEMITRI Y., Ph.D. Design of a Stark Microchip. (2015)
Directed by Dr. Liam M. Duffy. 106 pp.

The possibility of constructing scalable quantum computation systems in the near future is quite intriguing. Emergent systems based on polar molecules as qubits and quantum gates are considered among the most promising candidates. Controlled loading of the microtraps in a quantum-state-selective manner is a critical precursor to the formation and manipulation of qubits. This thesis details a design of a microchip capable of controlling the motion of molecules in high-field-seeking and low-field-seeking quantum states. The design is based on an alternative type of a Stark decelerator/accelerator, the so-called *type-B*, in which the electrode separation distance changes along the beam axis while the electric field switching time remains constant. Monte-Carlo simulation method shows that a 2-cm long device consisting of 100 stages can decelerate HCN-like polar molecules, in a phase-stable manner, from 200 m/s to a near standstill in about 150 microseconds. The same device can be operated 'in reverse' to accelerate stationary or slow moving molecules from microtraps. Two different types of geometries for alternating-gradient (AG) focusing of molecular motion are proposed. Comparison of the electric field distribution to the ideal harmonic field, as well as an analysis of the field magnitudes and gradients show that both geometries should be able to effectively decelerate or accelerate molecules while maintaining their transverse stability and focus. Finally, we propose a new technique for achieving longitudinal and transverse stability using only the accelerating fields. This new method is similar to the alternating phase focusing (APF) used in charged particle accelerators but applied to the case of polar molecules.

We showed using 1D trajectory simulations that this technique is capable of decelerating molecules in a phase-stable manner, but were unable to confirm transverse focusing.

DESIGN OF A STARK MICROCHIP

by

Demitri Y. Balabanov

A Dissertation Submitted to
the Faculty of the Graduate School at
The University of North Carolina at Greensboro
in Partial Fulfillment
of the Requirements for the Degree
Doctor of Philosophy

Greensboro
2015

Approved by

Committee Chair

APPROVAL PAGE

This dissertation written by Demitri Y. Balabanov has been approved by the following committee of the Faculty of The Graduate School at The University of North Carolina at Greensboro.

Committee Chair _____
Liam M. Duffy

Committee Members _____
Shyam Aravamudhan

_____
Daniel J. C. Herr

_____
James G. Ryan

_____
Date of Acceptance by Committee

_____
Date of Final Oral Examination

ACKNOWLEDGMENTS

I would like to thank my advisor Prof. Liam Duffy for his care and guidance in all three years of this thesis project. I would also like to extend my gratitude and thanks to Prof. William Gerace. This thesis would not have been possible without his continued support, encouragement and belief in my ultimate success.

Many Fridays in my first and second year at JSNN were spent discussing inventing and inventions with Prof. James Ryan. I'm grateful to him for taking the time to critic my ideas and for providing valuable insights. Special thanks is due to Prof. Joseph Starobin with whom I spent the first two years working on models of neuron activity.

Lastly, I'm forever grateful to my family and friends for their understanding and support.

TABLE OF CONTENTS

Page

LIST OF TABLES

Page

LIST OF FIGURES

Page

CHAPTER I

QUANTUM COMPUTING AND POLAR MOLECULES

The motivation for the work presented in this thesis is the possibility of constructing systems capable of quantum computation. We still do not know the ultimate computing capability of classical machines but we do know the ultimate physical bounds for miniaturization of their 'hardware.' It is significant that this year marks the 50^{th} anniversary of Moore's 'law' for the rate of decrease of the size of the transistors. Since 1950s, transistors became the main elements of the semiconductor electronics and the building blocks of the classical computers. Decreasing their physical size allows to fit more transistors per unit of area, which increases the functionality and computational power of the machine. However, the size of the modern transistors is already so small that undesired quantum effects begin to interfere with the functioning of the logic gates. In a laboratory setting, the lower limit of miniaturization has already been reached with the fabrication of single-atom transistors [1][2].

Instead of trying to fight a doomed battle against quantum mechanics, quantum computers embrace it and in so doing change the nature of computation itself. In an ordinary classical computer, all of the bits have a definite state at any instant in time, for example $01111000\ldots$ But in a quantum computer the state of the bits is described by a properly normalized wave function, such as $\Psi = a|01111000\ldots\rangle + b|01111001\ldots\rangle + \cdots$ where the coefficients are complex numbers. The probability that a computer is in state 01111000 or 01111001 is given by the product of the corresponding probability amplitude and its complex conjugate a^*a or b^*b, respectively.

The difference between quantum computing and the probabilistic classical computing is in the fact that the coefficients (probability amplitudes) reside in the complex plane, that is, they have both a magnitude and a phase. As it turns out, the phase difference is a meaningful parameter describing the interference between different states of the computer, a very useful process for computation. Hence, a quantum computer's advantage lies in the fact that it can be in multiple states at once (superposition principle) and that it can act on all of its states simultaneously achieving massive parallelism. This allows a quantum computer to solve problems that are beyond computational powers of any current or future classical (super) computers and to do all of that with a relatively few number of quantum bits (qubits).

The idea of quantum computer is simple but its physical realization is much less so. We do know a set of basic criteria that a quantum computation device must satisfy [3]. It must be a scalable physical system with well-characterized qubits, the quantum state of such system should not rapidly degrade (long decoherence times), one must be able to bring the system to some initial state (initialization), to perform logical operations with qubits and pairs of qubits (universal operations), and to reliably measure the system's final state. Almost any quantum mechanical system can be used as a qubit and this freedom is reflected in the large number of candidate quantum computation platforms proposed or pursued by scientists around the world. From a practical point of view, solid-state systems such as those based on quantum dots [4][5], nitrogen vacancies in diamond [6] or Josephson junctions [7][8] are all interesting candidates. However, in such systems it is particularly hard to prevent (reduce) decoherence of the quantum system due to an inherent coupling to the solid environment. Fortunately, decoherence does not need to be completely eliminated but only

lowered to a certain threshold at which point quantum error correction operations dominate, resulting in fault-tolerant quantum computation [9].

Among the possible platforms, a special attention is devoted to quantum optical systems based on trapped ions and neutral atoms. Such isolated systems have excellent coherence properties resulting in very reliable qubits. Controlled interaction among these qubits can produce reliable quantum logic gates. Optical pumping can be used for initialization and final state measurement with nearly 100% efficiency, through the use of state-dependent optical fluorescence detection [10]. Ions are attractive from an experimental point of view because of their strong coupling to the electric field via Coulomb's law. This makes them easy to manipulate with electric fields even to achieve nanometer precise confinement [11][12]. At the same time, this sensitivity makes the use of ions difficult to scale to larger systems. Neutral atoms do not couple as strongly to the electric field and therefore do not have the same Coulombic repulsion problem faced by the ions. But, as a result of such weak coupling, attaining the necessary interaction between the qubits is difficult. Neutral atoms must be brought together using lasers in order to achieve entanglement through contact interactions [13] or be promoted to Rydberg states in order to produce large dipole moments that can then couple strongly to the field [14]. In either case, this makes them also difficult to scale to larger systems while retaining the coherence and control demonstrated in small systems. The use of lasers for trapping and manipulation presents a difficulty in integrating such systems with electrical circuits.

An emergent quantum-computing platform based on polar molecules can perhaps overcome the above-mentioned difficulties. Unlike atoms, molecules possess asymmetry in their structure. From this asymmetry and with the application of an electric

field, molecules can acquire large dipole moments (on the order of a few Debye) that are comparable to the transition dipole moments of optical atomic transitions [15] but typically smaller than the dipole moments associated with Rydberg states. These dipole moments are a key distinguishing feature that allows a tunable coupling to the electric field. As a result, an almost complete control of the molecule's internal and external degrees of freedom can be achieved using DC or microwave-frequency electric fields. Controlling such fields with high precision is readily attainable even with current technologies making it feasible to integrate polar molecule based quantum computation systems with microelectronic circuits [16]. Molecules have a rich internal state structure with a variety of long-lived hyperfine and rotational states that, similar to quantum dots and superconducting flux qubits, can be controlled with electric fields. Using arrays of such molecules is especially promising since the scaling to larger networks of coupled qubits seems to be relatively straightforward [17][18][15][19]. The tunable coupling between the qubits is achieved with dipole-dipole interactions, the long nature of which can make the coupling effective even at moderate distances. Since the speed of the logic gates is proportional to the strength of these interactions, it seems possible to design fast logic gates even between remote qubits [16]. Although the quantum computation platform based on polar molecules is a relatively new direction it has attracted much attention in the scientific community and is considered to be among the most promising platforms to implement a quantum computer [20].

All envisioned quantum computation schemes involving polar molecules require first trapping the molecules that are in very specific quantum states (for example, rotational states of a molecular electronic ground state). In general, molecules can

be in low-field-seeking (LFS) quantum states or in high-field-seeking (HFS) quantum states and which of those two types of states it is in, determines the way in which that molecule interacts with the electric field. A variety of traps for polar molecules have been proposed and/or implemented. From the technological point of view, manipulating and trapping molecules in LFS states is much easier and has already been demonstrated with macroscopic [21][22][23] and microscopic electrostatic traps [24][25][26][27][28][29]. Since it is impossible to create an electric field maximum in free-space, trapping and guiding molecules in HFS states is more difficult but possible. To do that, requires using not static electric fields but time-dependent fields where a time-averaged electric field local maximum can be created. Macroscopic electric traps of this kind have already been proposed and built [30][31][32][33][34][35][36][37]. Several microscopic trap designs have been proposed [38][39] but as of yet, none have been built. It should be noted that such electrodynamic traps are more versatile, capable of trapping atoms as well as molecules not only in HFS states but also LFS states. Completely different types of traps are also possible such as magnetic traps [40][41][42], microwave traps [43] and optical traps [44]. We point out that electrostatic traps (or quasistatic traps in general) have an advantage over the optical traps in that the transitions between stationary states are unlikely (except for Majorana transitions).

Efficient loading of the traps requires control of the motional degrees of freedom of the molecule. Typical traps are relatively shallow which means that the kinetic energy of the approaching molecule needs to be low enough that it would not escape the electric trap. Consequently, in addition to the traps that ultimately hold polar molecule qubits, a mechanism is needed for reducing the kinetic energy (slowing

molecules down) and for guiding the molecules to the trapping sites. This control of the molecular motion can be most efficiently accomplished with time-varying inhomogeneous electric (or magnetic) fields.

From a historical perspective, a control of the transverse motional degrees of freedom of a neutral atom was first achieved in the early days of 1920s. It wasn't until a decade and a half ago, in the late 1990s, that a full control of the longitudinal motion of the molecules, in a molecular beam, became practically possible. Of course, in the context of the molecular or atomic beams, the mean forward velocity of the beam can be varied by adjusting the temperature of the source or by using various seed gases. However, the more precise control over the longitudinal motion was not possible until the development of the so-called Stark deceleration technique and its experimental demonstration in 1999 [45]. Subsequently many molecules in LFS states have been decelerated and guided. To do likewise with the molecules in HFS states, a technique was borrowed from the charged-particle physics, called Alternating-Gradient (AG) focusing, and modified to work with neutral particles [46][47]. However, both Stark decelerators for LFS molecules and AG decelerators for LFS/HFS molecules used thus far are very large, ranging from approximately 0.5 meters to 2.5 meters [48]. Such large sizes make them very difficult to integrate with microelectronics and to act as a component of a viable quantum-computing platform. In fact, their large sizes are derived from two major reasons: first, their application is in molecular beam studies where having large densities and numbers of particles is typically preferred and second, they are built using lathes and assembled with human hands which means that there is a practical lower limit to how small they can get ($\sim$ tens of centimeters).

In order to be used for guiding and loading microtraps, in a controlled manner, these decelerators need to be miniaturized.

Advances in micro- and nanofabrication make miniaturization of devices like molecular decelerators and charged-particle accelerators possible. In 2009 the first microchip Stark decelerator was built [24]. However the microchip has a few limitations that render it unattractive as a component of a quantum-computation system. First, the microchip can only decelerate/accelerate molecules in LFS states whereas molecules in their ground state, which is always HFS, are desirable. Second, the moving potential wells are quite shallow making the deceleration/acceleration process inefficient. Third, the integration with microelectronics is still problematic since to operate the device requires custom made high-voltage ($\sim$ 200 Volts) amplifiers using pentode vacuum tubes and a high frequency op-amps [49]. A few years later in 2013 the first and, so far, the only microchip charged-particle accelerator was built capable of accelerating electrons at a rate 10 times higher than conventional macroscopic particle accelerators [50]. In both instances mentioned above, miniaturization, aside from making the device small and compact, improves the functioning due to the production of high field gradients. The force experienced by a neutral particle in an inhomogeneous electric field is proportional to the gradient of that field. Consequently, there is a clear advantage in pursuing miniaturization if control of motional degrees of freedom is desirable. Ultimately, miniaturization allows building on planar substrates using lithographic techniques with atomic-scale positioning and alignment which also makes it possible to integrate several different devices (like microtraps, guides, etc.,) on the same chip.

This dissertation describes how a viable microchip capable of controlling the motion of molecules in HFS and LFS states may be designed. Such a device is an important enabling component of the proposed quantum computing platforms based on polar molecules since it allows controlled loading of the microtraps in a quantum-state-selective manner — a critical precursor for subsequent formation and manipulation of qubits.

Of course, before molecules can be slowed down and trapped they first need to be produced. In Chapter 2 we present two techniques for production of molecules with a well-defined kinetic energy and low internal temperatures: supersonic expansion and buffer-gas cooling. We calculate the expected parameters such as longitudinal speed and velocity spreads that are subsequently used as initial conditions in our simulation programs. A detailed understanding of the particle dynamics inside a device can be obtained from the trajectory simulations. We created two different types of simulation programs, CoMP1 and CoMP2, that run on top of SIMION® and are used for creating electrode geometries, calculating three-dimensional electric fields, field gradients, forces and trajectories. Once a Stark microchip is fabricated its functioning will need to be assessed. A possible experimental setup is proposed where we combine the resonance enhanced multiphoton ionization (REMPI) detection method with the Doppler shift measurements using the mm-wave (microwave) beam.

The microchip design presented in Chapter 3 is based on an alternative type of Stark decelerator/accelerator, the so-called *type-B*, in which the electrode separation distance changes along the beam axis while the electric field switching time remains constant. This design is advantages over the typical Stark decelerator design in that it can produce cold, continuous or quasi-continuous molecular beams while using simpler

electric field pulse timing. The results of 1-dimensional trajectory simulations show that 2 cm device consisting of 100 stages can decelerate molecules, in a phase-stable manner, from 200 m/s to a near standstill in about 150 microseconds. We also show that the same device can be used 'in reverse' to accelerate stationary or slow moving molecules loaded in traps.

Over the past decade, many different electric and magnetic field geometries have been proposed to affect the transverse motion of polar molecules. In Chapter 4, we begin by describing the theory of AG focusing and how a suitable electrode geometry may be found using an analytical approach based on the multipole field expansion. In order to achieve focusing, the gradient of the electric field has to be periodically rotated by 90 degrees. We propose two different types of geometries capable of transverse focusing and analyze the resultant fields. It is found that both geometries should be able to effectively decelerate or accelerate molecules while maintaining transverse stability and focus. However, further studies using 3D trajectory simulations should be performed to confirm this conclusion. The general motion of the particle inside an AG device is comprised of a micromotion superimposed on a macromotion. A brief analysis of the transverse motion of a molecule in an alternating gradient setup is presented assuming harmonic interaction potential and a constant effective dipole moment. The resultant equations of motion are of Mathieu-Hill type which can be solved exactly for a piecewise constant waveform. Finally, we propose a new technique for achieving longitudinal and transverse stability using only the accelerating fields. This new method is similar to the alternating phase focusing (APF) used in charged particle accelerators but applied to the case of polar molecules. We showed using

1D trajectory simulations that it is possible to decelerate molecules in phase-stable manner using this technique but were unable to confirm transverse focusing.

CHAPTER II

DECELERATION AND ACCELERATION OF POLAR MOLECULES ON A MICROCHIP

The majority of the experimental efforts in Stark deceleration have focused on molecules in low-field seeking (LFS) quantum states. This is due to a number of technical challenges associated with efficient guiding, trapping and manipulation of molecules in high-field seeking (HFS) quantum states. From a scientific and a technological point of view, molecules in HFS states are a very promising system to work with for two major reasons. First, the ground state of any molecule is always high-field seeking with respect to an external perturbation. Ground states, in turn, are desirable due to their long lifetimes. Working with such a system could make it possible to create molecular Bose-Einstein condensates in traps. This does not seem to be possible with LFS states due to undesirable collisions. Second, the quantum states of large molecules become high-field seeking in relatively small electric fields and all states become HFS given a high enough electric field. Therefore, if it was possible to efficiently bring such a system to a cold (or ultracold) regime, while retaining the control over the molecules, then the system would be a promising platform for quantum information processing. However, the integration of molecular systems, HFS molecular systems in particular, with solid-state devices remains challenging.

In this chapter we present results on one-dimensional (1D) deceleration and acceleration of the ground-state HCN-like molecular beam using a Monte-Carlo simulation method. Deceleration (acceleration) is achieved using an alternative type of Stark

decelerator (accelerator), the so-called *type-B* [51], in which the electrode separation distance changes along the beam axis while the electric field switching time remains constant. This type of a device is in contrast to the commonly used *type-A* Stark decelerator in which the electrode separation distance is kept constant while the electric field switching time is varied.

The advantages offered by the *type-B* Stark decelerator are the ability to produce cold, continuous or quasi-continuous molecular beams while using simpler electric field pulse timing. The miniaturization of the electrodes to the micrometer-scale enables the production of high electric field gradients using low voltages that are compatible with voltages used in microelectronics. Finally, the use of modern micro- and nanofabrication methods make possible the fabrication of electrodes with more precise alignment and tailored geometries. This is important because achieving precise electrode alignment, in particular, is the biggest technological hurdle limiting the efficiency of the current macroscopic alternating-gradient (AG) decelerators for polar molecules [52]. Additionally, electrode 'shaping' can maximize phase-space acceptance of the decelerator and result in more favorable beam dynamics. Both the improved alignment and the electrode shaping would give greater control over the molecule's motional degrees of freedom.

2.1 Type-B Microstructured Accelerator-Decelerator

In principle one can devise arbitrarily complex electrode geometry to decelerate the molecular beam. Choosing a particular geometry determines the boundary conditions to the Laplace equation and therefore determines the electric field distribution. Knowing the spatial distribution of the electric field and the quantum state of the molecules inside the beam (and hence, the dependence of the Stark energy on the elec-

tric field) enables one to calculate numerically the force experienced by the molecules at any point inside the device. For simplicity we chose an electrode geometry that does not change in one of the transverse directions (along x-axis). We neglect the edge effects due to fringe fields by extending all edges to infinity thus making our electrode geometry effectively two-dimensional (2D).

The shape and arrangement of the electrodes are illustrated in Figure 1. Two parallel, conductive plates are separated by a distance $d = 25\mu m$. The inside surfaces of the plates are modulated by a set of parallel, interconnected microstructures that span the entire width of the device (Figure 1a). When a constant-period, square wave potential difference pulse is supplied to the plates (Figure 1c), these microstructures, which we call electrodes, produce regions of non-uniform electric field along the z-axis that decelerate polar molecules. To be consistent with the literature we define such regions as field-stages. These microstructures act in a similar way as the electrodes in a conventional Stark or alternating-gradient (AG) decelerators except that we shape the electrodes to yield a particular longitudinal electric field distribution. The exact shape of the electrodes determines the curvature profile of the resultant Stark (potential) energy hill and hence, determines the forces experienced by the molecules (Figure 1b). Note that, in principle, all electrodes could be insulated from each other and therefore be independently controlled. In particular, if the last stage is separate from all the other stages then a final (exit) beam velocity can be dialed by supplying that stage with an appropriate voltage.

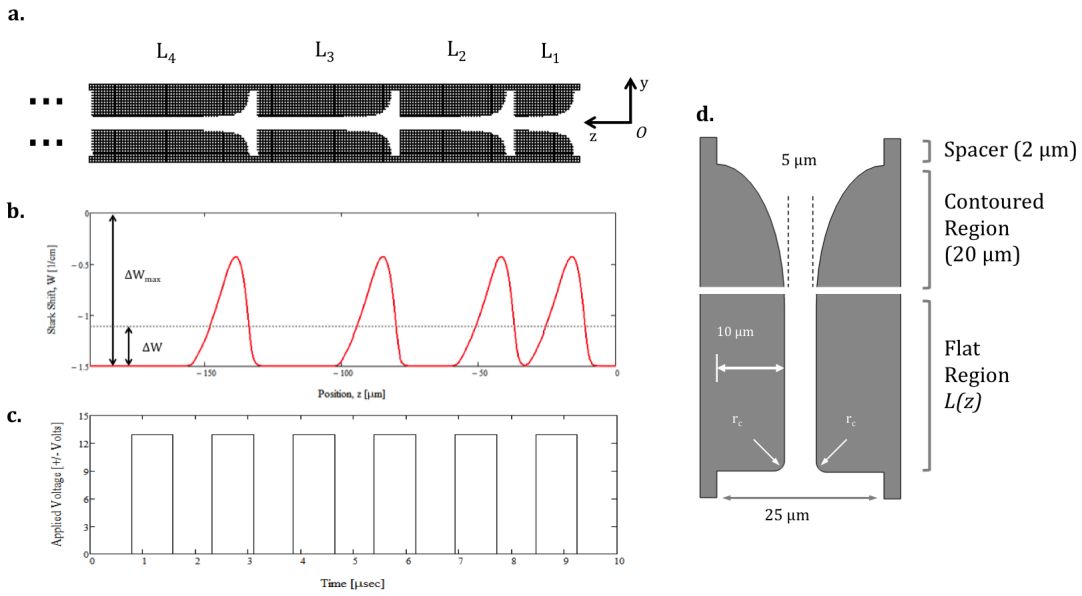

Figure 1. Microstructured Type-B Accelerator-Decelerator for the Polar Molecules. (a) Layout of the Type-B accelerator-decelerator for the polar molecules, showing the first four stages, in the case of acceleration, or the last 4 stages, in the case of deceleration. The lengths of the stages, L_j, must either increase (acceleration) or decrease (deceleration), relative to the molecule's starting position, in order to have a constant electric field switching time. (b) Potential energy along the z-axis for HCN-like molecule in a ground ro-vibrational state (HFS). (c) The first 6 cycles of a constant-period, square-wave pulse sequence (d = 0.511, T = 1535.4 nsec) of $\pm$12.95 Volts applied to the decelerator. (d) Schematic view of a single stage. See text for details.

Figure 1d shows a schematic of a single stage. It is comprised of two connected regions: a fixed length contoured region and a variable length, $L(z)$, flat region. The shaping of the electrodes is accomplished by supplying a contour function that determines the exact geometry inside the contoured region. One is free to choose any contour function. For practical reasons, the contour function used in our experiments is a truncated right hyperbola. We've set the total length of the shortest stage to be $L_1 = 20\mu m$ and have limited the smallest feature size on the device to $1\mu m$ for ease

of fabrication by lower-cost micro- and nanolithography techniques. A $5\mu m$ opening between the plates, through which the molecular beam propagates, was modeled recognizing that the requisite electric field strengths of 50–100 kV/cm can then be achieved with conventional, commercially available, pulse generators operating at approximately ± 15 Volts. We note that higher separation distances can easily be used but would require supplying higher voltages. The stages are terminated with a $10\mu m$ perpendicular drop, which is also the width of the contoured region. Varying this width allows us to tune the electric field local minimum and therefore control the height of the potential energy hill seen by the molecules. All corners of the electrodes are rounded off with 1/4 circle of radius $r_c = 1\mu m$.

In order to keep the electric field switching time constant we vary the length of the flat region, $L(z)$, while keeping the contoured region's length constant for all the stages in the device. In the case of deceleration, the kinetic energy decreases linearly with each stage while the velocity decreases approximately as the square root. Therefore, in order to use constant-period ON/OFF pulse, the ratio of the electrode length to the velocity of the synchronous particle in that stage must remain constant. Consequently, the length of the electrodes must be proportional to $L_j \propto \sqrt{j}$, where j is the index number of the j^{th} stage This formula assumes that a synchronous molecule stops after traversing the last set of electrodes and that the molecule receives an instantaneous impulse that reduces its velocity (see Section 2.2). Figure shows how the lengths of the stages must vary along the beam axis when the decelerator is driven by the constant-period, square-wave pulse shown in Figure 1c. The total length of this 100-stage decelerator is about 20.5 mm.

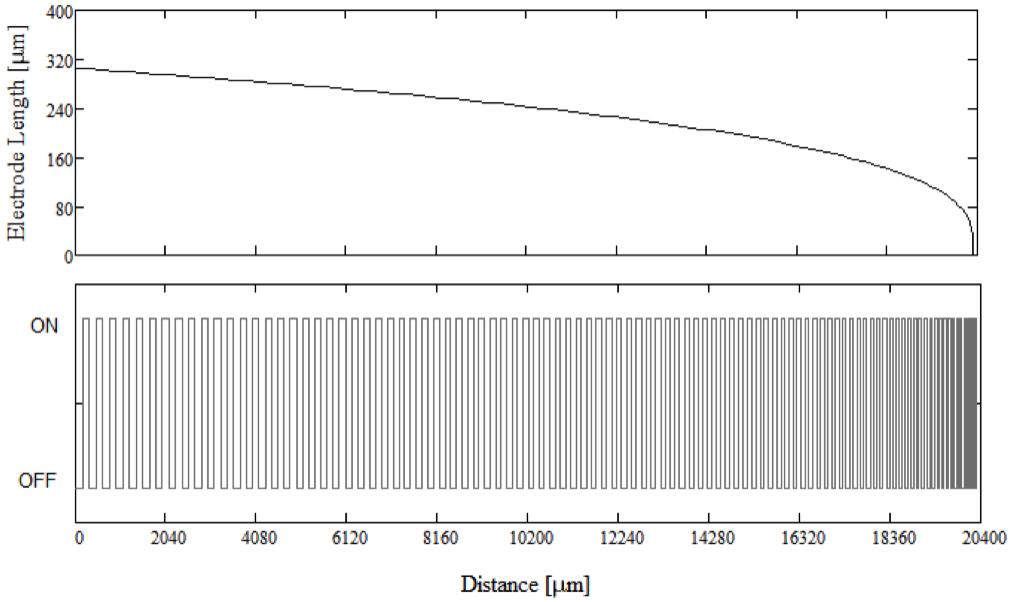

Figure 2. Electrode Length as a Function of Distance. The upper panel shows the electrode length as a function of distance, z, from the decelerator's entrance. The curve was obtained from Equation 2.3. Distance covered by a synchronous molecule during the time when the field is ON (t_{on} = 785.4 nsec) and when the field is OFF (t_{off} = 750 nsec) is depicted in the lower panel. The total distance covered by the molecule during one period (T = 1535.4 nsec) is equal to the length of the corresponding stage. The longest stage is approximately 305 μm and the shortest is 20 μm. The total length of the decelerator is about 2 cm.

2.2 Experimental Results of 1D Simulation

The calculations were performed using the latest version of SIMION®, a charged particle optics simulation software, which we have modified to work with polar molecules. The parameters of the simulation particles were equated to the physical parameters of hydrogen cyanide (HCN). In particular, HCN is a simple linear tri-atomic molecule with a relatively large dipole moment of 2.98 Debye in its ground state [53], molar mass of 27.03 g/mol and a rotational constant of 44315.975 MHz/c. HCN is also

an attractive molecule for manipulation with mm-wave techniques. The simulated particles were assumed to be in a ground ro-vibrational state (HFS).

To estimate the resultant Stark shift and the effective dipole moment we've used a high-field, pendular-state model [54]. In this model the Stark shift, W, and the effective dipole moment may be expressed as:

$$\frac{W(v_p, \lambda)}{B} = -\lambda + (v_p + 1)\sqrt{2\lambda} \tag{2.1}$$

$$\mu_{eff} = \mu\left(1 - \frac{v_p + 1}{\sqrt{2\lambda}}\right) \tag{2.2}$$

where $\lambda = \mu E/B$ is the dimensionless parameter relating the body-fixed dipole moment μ and the rotational constant, B, of an idealized rigid-rotor molecule interacting with the electric field E. Application of the electric field readily mixes different angular momentum quantum states J. Therefore, in the strong-field limit ($\lambda >> 1$), the pendular states must be characterized by the quantum numbers v_p and M (projection of J onto the field axis) with $v_p = 2J - |M|$. In this limit, the body-fixed dipole moment is essentially parallel to the applied electric field and all the low-lying states are HFS. Furthermore, for small changes in the electric field, the effective dipole moment can be approximated as constant.

2.2.1 Deceleration

In general, molecular species require different deceleration voltages depending on their initial kinetic energy and Stark shift. Applying ± 12.95 Volts to the electrodes would result in a maximum electric field of 51.78 kV/cm along the beam axis. At

such electric fields HCN-like molecule's effective ground-state dipole moment is equal to 1.39 Debye with the total high-field limit Stark shift of about $\Delta W_{max} = 1.81$ cm^{-1} (or 0.224 meV). In order to decelerate a bunch of molecules from an initial longitudinal speed of $v_0 = 200$ m/s to a complete stop using $n = 100$ stages requires each field-stage to extract $\Delta E = \frac{1}{2}mv_0^2/n$ of molecule's kinetic energy. For HCN-like particle this equals to 0.451 cm^{-1} (at $\Delta W/W = \alpha = 0.25$). As the molecules propagate through the device we cycle the electric field from configuration-1 ("ON") for the duration of $t_{on} = 785.4$ nsec, to configuration-2 ("OFF") for the duration of $t_{off} = 750.0$ nsec. It is convenient to speak of the duty cycle, d, when characterizing the time dependence of the applied field configuration. The duty cycle is defined as the fraction of the period during which configuration-1 is applied i.e. $d \equiv t_{on}/(t_{on} + t_{off})$, which, for this experiment, equals to 0.511.

In order to confirm that electrodes have the proper spacing, we inject a monochromatic beam of molecules and monitor the phase-space dynamics of the deceleration process. Initially molecules are distributed uniformly along the beam axis, over the entire length of the first stage, with a longitudinal speed of 200 m/s (see Figure 3). As the molecules move through the device a certain subset of the initial molecular distribution is gradually decelerated to about 5 m/s after traversing 100 stages. Due to phase stability the molecules within this bunch are held together, maintaining a narrow spatial and velocity spread throughout the deceleration process. The inserts of Figure 3 show the initial molecular distribution at stage-1 and a phase-space bucket at stage-91 enclosed by an ellipse. Molecules within the ellipse execute elliptic, non-overlapping trajectories around the synchronous molecule located at the center.

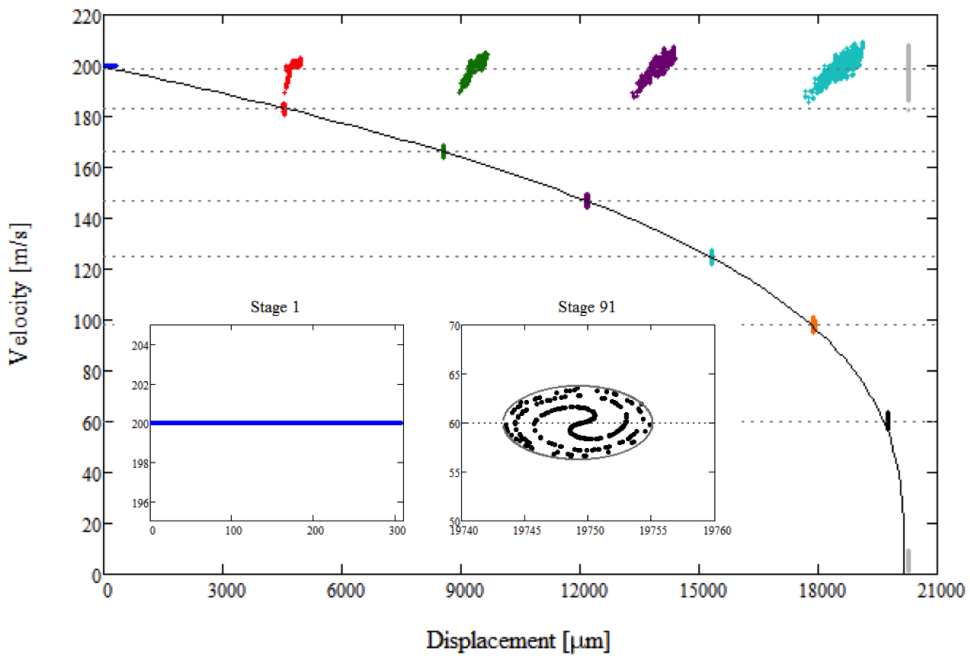

Figure 3. Phase-Space Plot of the Deceleration Process for a Ground State, HCN-like Monochromatic Molecular Beam. A small subgroup of the initial distribution, shown in the insert, forms a bunch and is slowed down in a phase stable manner. Black (solid) curve is a theoretical prediction for the velocity and position of the synchronous molecule in the instantaneous impulse approximation. Horizontal (dashed) lines correspond to the expected velocities of the synchronous molecule at various stages. Data is recorded at stages 1 (blue), 16 (red), 31 (green), 46 (purple), 61 (teal), 76 (orange), 91 (black), 100 (grey). The last recording contains only the velocity information as it was recorded at a single point, along the z-axis, corresponding to the end of the decelerator.

Molecules located outside of the ellipse are not amenable to a phase-stable deceleration and are considered 'lost', pulling further ahead of the decelerated bunch. It should be noted that our last recording, at the end of stage-100, is meant to simulate a molecular beam hitting a CCD plate detector, which is fixed at the end of the device. Hence, the last recording produces only the time and velocity data.

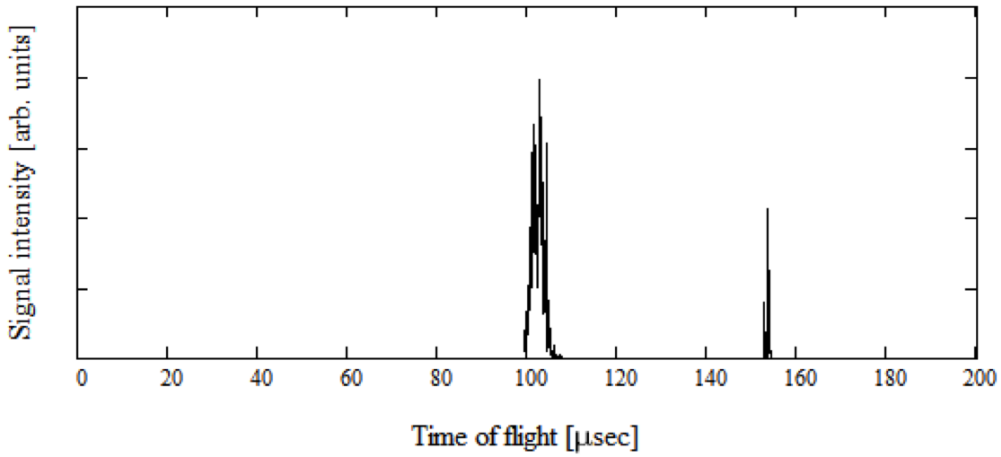

Figure 4. Time-of-Flight (TOF) Distribution of the Ground-State HCN-like Molecular Beam with an Initially Uniform Spatial Distribution and a Starting Velocity of 200 m/s. The second peak at around 153 μsec corresponds to the arrival time of the decelerated bunch. The vertical dashed line indicates an expected arrival time of a molecule flying with a constant speed of 200 m/s.

The acceptance of the decelerator corresponds to only a small fraction of the initial distribution (7%). Therefore, for most of the molecules the spacing of the electrodes and the field timing sequence will result in no significant (net) acceleration or deceleration. This molecular group, being largely unaffected by the presence of the deceleration stages, maintains the initial speed of 200 m/s although with an increasing velocity and spatial spread. This is clearly seen in the time-of-flight (TOF) distribution in Figure 4. A molecule flying with a constant speed of 200 m/s would take about 102 microseconds to exit a 2.04 cm long decelerator, which corresponds to the mean arrival time of this molecular group (the first peak in Figure 4). The smaller, decelerated bunch arrives at the exit after about 153 microseconds (the second peak in Figure 4).

Also plotted in Figure 3 are the expected velocities assuming 0.451 cm^{-1} reduction in the kinetic energy per stage (dashed lines) along with the theoretical predictions (solid line) for the speed and position of the synchronous particle using an impulse approximation. In this approximation it is assumed that the synchronous particle receives an instantaneous reduction in its kinetic energy, equal to ΔE, each time an electric field is turned ON. The position of the synchronous particle, at electrode j, can then be easily calculated using:

$$x_j = x_0 + (t_{on} + t_{off}) \sum_{k=1}^{j} \sqrt{v_0^2 \mp k \frac{2}{m} \Delta E} \tag{2.3}$$

where x_0 is the starting position relative to the origin, v_0 is the initial speed of the synchronous particle whose mass is m; $j = 1$ is the first stage encountered by the molecule and $j = 100$ is the last stage. Positive sign is used in the case of acceleration and negative in the case of deceleration. Since there is no information regarding the shape of the potential hill in Equation 2.3, the above formula is general and may be used for various electrode geometries.

It should be kept in mind, however, that the approximation tends to be less accurate as the electrode lengths decrease. Since the electric field inhomogeneity arises from the shape of the electrodes in the contoured region, therefore, we would expect the impulse approximation to be more accurate for longer electrodes in the beginning of the decelerator. Figure 5a shows the percentage of the electrode length occupied by the 20 μm contoured-region. In the first 50 stages, contoured region makes up less than 10% of that stage's length. Consequently, the time over which the molecule experiences a force can be considered to be a small fraction of the total

time it takes to cover the length of the electrode (one time period, T). In the last few stages a contoured region makes up a significant fraction of the total electrode length. It comprises 100% of the 100^{th} stage. Therefore, the impulse approximation will be worse for stages 50–100 and especially in the last few stages.

The difference between the actual position and the theoretically predicted one, expressed as a percentage of the corresponding stage length, is shown in Figure 5b. By stage 50, the overestimation of the actual position of the synchronous particle is less than 15% of that stage's length; however, by stage 91 the overestimation is equal to the entire length of that stage. Therefore, one would expect electrode lengths in the last few stages to no longer match the implemented deceleration scheme, resulting in creeping of the decelerated bunch into the next stage(s). The error will keep accumulating with longer decelerators unless a proper spacing of the stages is obtained. In general, the shape of the (Stark) potential energy hill is directly related to the particular geometry of the electrodes and must be determined numerically. To get a better analytical formula for the electrode spacing one can approximate the potential hill to be quadratic with respect to the displacement. However, even this approximation becomes increasingly inaccurate as the particle's speed decreases and the fraction of time spent traversing the inhomogeneous E-field region becomes comparable to (or greater than) the time spent outside of it. Having an accurate (numerical) solution for the Stark energy hill from the chosen electrode geometry would allow one to properly account for the particle's transit time within each stage and thus obtain the required stage spacing.

As mentioned above, particles comprising the initial phase-space filament execute elliptical trajectories inside the bucket, delineated by the phase-space ellipse.

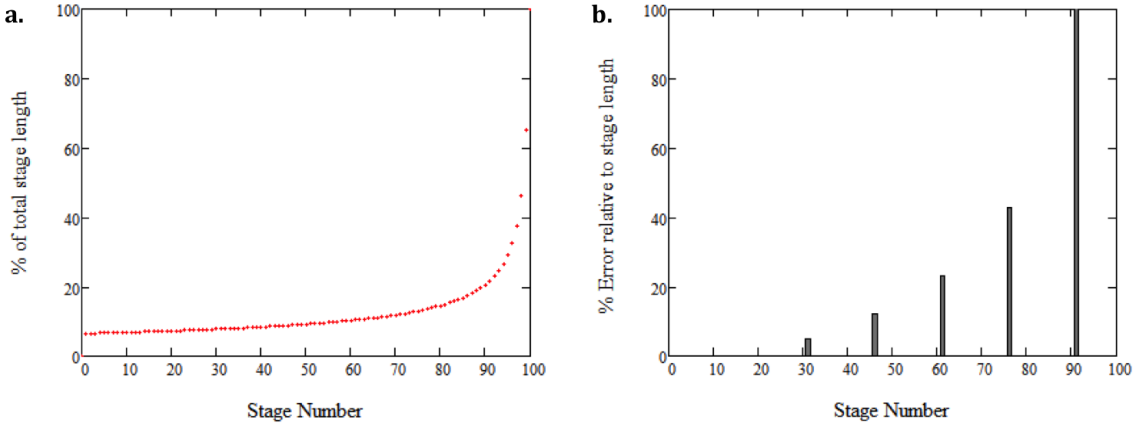

Figure 5. Comparison Between the Actual Position of the Molecule Inside the Device and the Theoretically Predicted Position. (a) Percentage of the electrode length occupied by the 20 μm contoured-region. (b) The difference between the actual position and the theoretically prediction one, expressed as a percentage of the corresponding stage length.

Since only conservative forces are involved in the deceleration, the phase-space area must remain constant via Liouville theorem (Figure 6a). Hence, minimizing the spatial spread maximizes the velocity spread and vice versa. In the phase-space representation this can be seen as a 90° rotation of the phase-space distribution. In Figure 6b, we plot the phase-space ellipses corresponding to stage 16 (red), 31 (green), 46 (purple), 61 (teal), 76 (orange) and 91 (black). Gradual reduction in the spatial spread and the concomitant increase in the velocity spread are clearly observed.

Another way of seeing this rotation is to simulate a molecular beam that has not only spatial distribution but also a uniform velocity distribution from 195 m/s to 205 m/s (see Figure 7). The plot for stage 1 shows that the phase-space acceptance of the device lies well within the initial distribution.

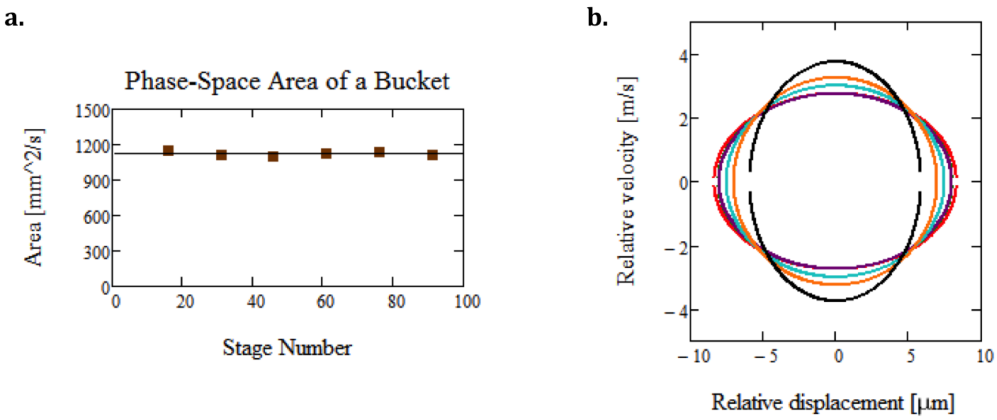

Figure 6. Phase-Space Area of the Decelerated Bunch. (a) Measured phase-space area of the decelerated bunch. (b) Gradual reduction in the spatial spread and the concomitant increase in the velocity spread for stages 16 (red), 31 (green), 46 (purple), 61 (teal), 76 (orange) and 91 (black).

Those molecules located outside of the acceptance region will eventually be lost from the decelerated bunch while resulting in a typical 'golf club' phase-space distribution (Stage 17). The bucket itself rotates uniformly in phase-space and can be made to assume any desired angle. For example, a rotation of 90° results in a maximum narrowing of spatial spread of the decelerated bunch.

This focusing in the forward direction, or "spatial bunching", of the molecular beam may be advantageous for experiments where it is desirable to increase the number density at a given point along the beam axis. This would include collision studies as well as loading of the decelerated beam into an electrostatic trap [55]. Alternatively, one can reduce the temperature of the decelerated beam by rotating the bucket such that the velocity spread is minimized. This would result in molecules keeping together for a longer period of time, albeit at an increased spatial separation.

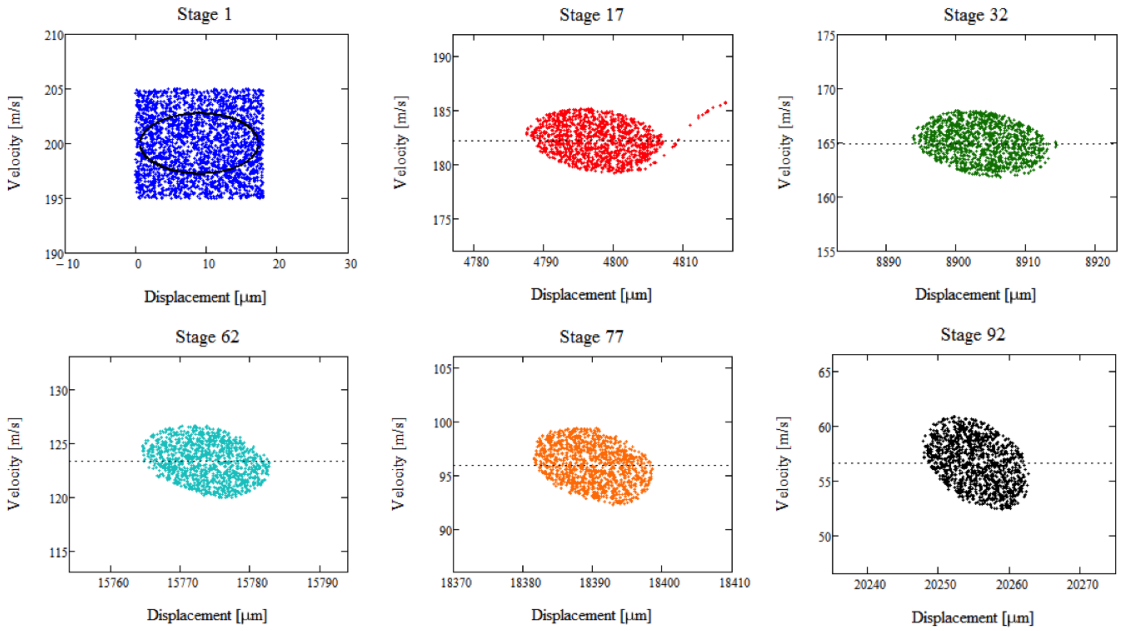

Figure 7. Phase-Space Plot of the Deceleration Process for a Ground State, HCN-like Molecular Beam with an Initial Uniform Velocity Distribution of 200 ±5 m/s, Recorded at Stages 1, 17, 32, 62, 77, and 92.

2.2.2 Acceleration

The topic of acceleration of polar molecules, in contrast to deceleration, has not been explored much. Yet a velocity-controlled acceleration (or re-acceleration) of a beam (or a group of molecules) is a relevant process for manipulation of neutral molecules. It may, indeed, prove useful to accelerate the molecules before decelerating them or to have acceleration-deceleration cycles in order to achieve some desired beam (ensemble) property. As an example, acceleration of polar molecules in a *type-B* accelerator gives rise to the phenomenon of phase compression, in the small-angle oscillation regime, which is absent in acceleration process of *type-A* device or in the deceleration of molecules in either *type-A* or *type-B* [51]. Acceleration of neutral molecules may also make it possible to use non-conservative forces, such as radia-

tion damping, to reduce the phase space volume occupied by the beam distribution, resulting in beam cooling. In 2004, prior to the development of the analytic "wave model" [56], Friedrich group published a paper on quasi-analytic model of a linear Stark accelerator-decelerator [51]. In it some of the dynamics underlying acceleration of polar molecules by *type-A* and *type-B* accelerators were examined.

Here, we present simulation results on acceleration of polar molecules. The scheme is similar to the one used in our deceleration studies where only conservative forces were involved. As before, the electrodes are activated for the duration of 785.4 nsec with a duty cycle of d = 0.5. In order to accelerate molecules from standstill to 200 m/s after passing through 100 stages requires each molecule to receive 0.451 cm^{-1} of the kinetic energy per stage. Figure 8a shows a phase-space plot of the acceleration process for a ground state, HCN-like molecular beam recorded at every 15^{th} stage starting from stage-1. As before, the molecules slam into the detector positioned at the end of the device. Most of the molecules in the initial phase-space filament (Figure 8b) are contained in the fastest, leading bunch while the rest of the molecules acquire slower velocities and form groups within a 'comet tail' like structure. The phase stability is maintained, for the leading bunch, throughout the acceleration process (Figure 8c).

Using an instantaneous impulse approximation, it is possible to predict the position and speed of the synchronous particle. The solid (black) curve in (Figure 8a is obtained using Equation 2.3 and agrees with the simulation results to within $\pm 2\mu$m.

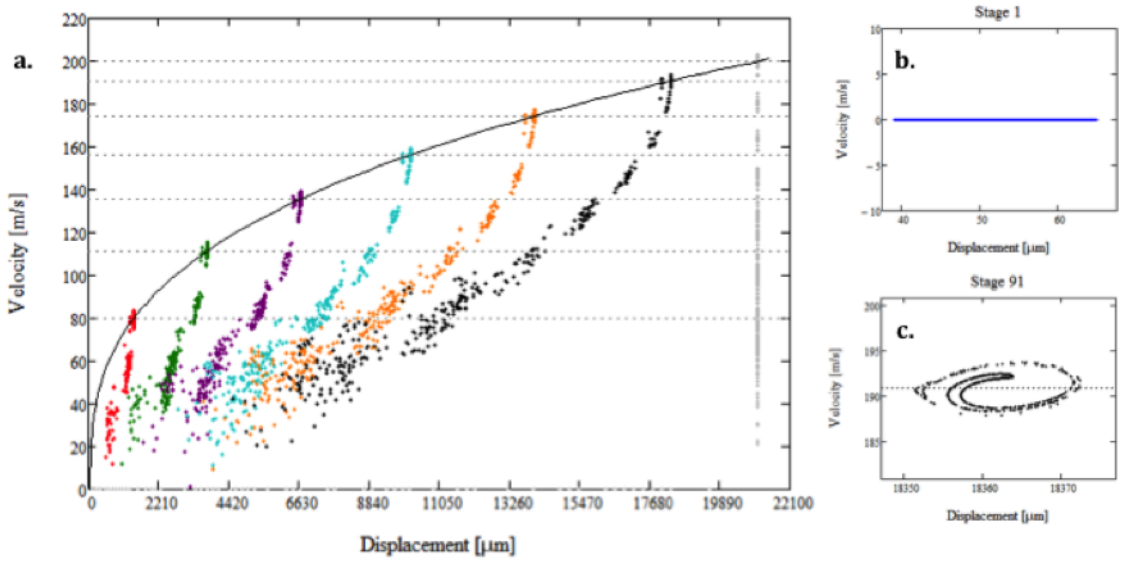

Figure 8. Phase-Space Plot of the Acceleration Process for a Ground State, HCN-like Molecular Beam with an Initial Uniform Spatial Distribution. (a) Phase-space plot of the acceleration process recorded at stages 1, 16, 31, 46, 61, 76, 91 and 100 using the same color scheme as before. Also shown is the theoretical prediction for the velocity and position of the synchronous molecule in the instantaneous impulse approximation (solid curve). Horizontal (dashed) lines correspond to the expected velocities of the synchronous molecule at the recorded stages. (b) In this simulation all molecules have an initial velocity of 0 m/s and are spread uniformly, along the beam axis, over the entire length of stage-1. (c) Molecules comprising the leading, accelerated bunch maintain phase stability throughout the acceleration process.

2.3 Conclusions

Stark deceleration of polar molecules is a versatile method for producing slow and cold beams. All of the decelerators thus far have been using *type-A* architecture where the electrode spacing is kept constant. In this chapter we presented simulation studies on an alternative, *type-B*, architecture where the electrode spacing changes in such a way so as to keep the electric field switching time constant, thus greatly simplifying the driving electronics. Building such a decelerator on a macro-scale (≈ 1 m) is much more challenging than building a *type-A* device due to variable electrode

spacing (lengths). However, miniaturization of the device to the micro-scale can readily achieve the desired spacing and electrode alignment using standard micro- and nanolithography techniques while making it possible to operate the device at low voltages. It also becomes possible to shape the electrodes in order to maximize the phase-space acceptance.

We show that a 2 cm decelerator consisting of 100 stages can bring molecules from 200 m/s to a near standstill in about 150 microseconds. To decelerate faster beams it is possible to use longer decelerators, utilizing more stages, or higher voltages. However, in order to effectively decelerate molecules to low speeds requires having an accurate numerical solution for the potential energy hills given particular electrode geometry. Ultimately, the proper electrode geometry and stage spacing should be done by an optimization computer code, similar to how it is done in designing particle accelerators where the entire beam transport line is simulated.

The same device can be used 'in reverse' to accelerate stationary or slow moving molecules loaded in traps. A phase-stable acceleration from 0 m/s to 200 m/s using 100 stages is possible. We suggest that the acceleration of molecules may be desirable for achieving certain beam properties, such as phase compression, before ultimately decelerating the beam. One can think of acceleration-deceleration cycles utilizing frictional forces that reduce velocity by radiation, resulting in beam cooling.

CHAPTER III

ALTERNATING-GRADIENT AND ALTERNATING-PHASE FOCUSING

Controlling transverse motion of the molecules in the low-field-seeking (LFS) quantum states with electrostatic multipole fields can produce focused beams. Such beams proved useful in the early days of molecular beam experiments. Gaining a similar control over the high-field-seeking (HFS) molecular states with electrostatic multipole fields however, is more challenging. The difficulty stems not from a technological limitation but a physical one: in a free space, Maxwell's equations permit an electric field minimum but not a maximum. Consequently, it is impossible to devise electrode geometry, no matter how clever, to hold HFS molecules in stable equilibrium with static fields alone.

The situation with HFS molecules is analogous to one in charged particle physics. According to Earnshaw's Theorem [57], an electrically charged particle (or magnet) placed in a static electric field (or static magnetic field) can not rest in a stable equilibrium under the influence of electrical (or magnetic) forces alone. Thus, no clever arrangement of charges, producing a static electric field, can result in a stable equilibrium for another charged particle. A different approach is needed to achieve stable equilibrium for such particles. In 1949 Nicholas Christofilos [58] devised a dynamic focusing scheme, for charged particles, that is now known as "strong-focusing" or "alternating-gradient (AG) focusing". Subsequent analysis extended the AG focusing scheme to the case of neutral particles (such as atoms, molecules and polar molecules) by Auerbach, Bromberg and Wharton [59]. Recently, this focusing scheme

was discussed in the context of AG deceleration [54] and AG focusing [60] of polar molecules. With an alternating-gradient setup molecules in LFS and HFS states can be successfully focused, transported and trapped.

3.1 General Principles of Alternating Gradient Focusing

This section describes how one may manipulate polar molecules with linear Stark potential energy using electric fields. It is assumed that molecules inside the device have velocity-independent (conservative) potentials so that the divergence of the force field is obtained from a scalar potential energy alone. It is further assumed that the electric field E is externally applied (by means of electrodes) and hence in a source-free region Maxwell's equation becomes:

$$\vec{\nabla} \cdot \vec{E} = 0 \tag{3.1}$$

Since there are no time-dependent magnetic fields one can express E as the negative gradient of a scalar potential φ that satisfies Laplace's equation $\nabla^2 \varphi = 0$:

$$\vec{E} = -\vec{\nabla}\varphi \tag{3.2}$$

In general, a particle can have stable (confined) trajectories in a space around $\vec{r} = \vec{r}_0 = 0$ if the applied force field $\vec{F}(r)$ vanishes at $\vec{r}_0$ and, for small spatial deviations, the applied force restores the particle's position towards $\vec{r}_0 = 0$. The latter requirement is true if it fulfills the necessary (but not sufficient) condition for confinement:

$$\vec{\nabla} \cdot \vec{F} < 0 \tag{3.3}$$

Molecules with Stark energy $W(E)$ in an inhomogeneous electric field of magnitude $E = |\vec{E}|$ experience a force:

$$\vec{F} = -\vec{\nabla} W(E) \tag{3.4}$$

For molecules that have a first-order interaction with the electric field (linear Stark shift), the Stark energy may be expressed as

$$W(E) = -\mu_{eff} E \tag{3.5}$$

The value of the effective dipole moment μ_{eff} depends on the particular quantum state of the molecule. Using equations (3.2), (3.4) and (3.5) the force on a molecule can be written in a component form

$$F_j = \frac{\mu_{eff}}{E} \sum_{i=1}^{3} \left(\frac{\partial \varphi}{\partial x_i} \right) \left(\frac{\partial^2 \varphi}{\partial x_i \partial x_j} \right) \tag{3.6}$$

The divergence of the force field $\vec{\nabla} \cdot \vec{F}$ can then be written as

$$\sum_{j=1}^{3} \frac{\partial F}{\partial x_j} = \frac{\mu_{eff}}{E^3} \sum_{i,j,k=1}^{3} \left[\left(\frac{\partial \varphi}{\partial x_k} \right)^2 \left(\frac{\partial^2 \varphi}{\partial x_i \partial x_j} \right)^2 - \left(\frac{\partial \varphi}{\partial x_i} \right) \left(\frac{\partial \varphi}{\partial x_k} \right) \left(\frac{\partial^2 \varphi}{\partial x_i \partial x_j} \right) \left(\frac{\partial^2 \varphi}{\partial x_k \partial x_j} \right) \right] \tag{3.7}$$

Using Schwartz's inequality

$$\left(\sum_{j=1}^{n} x_i y_i \right)^2 \leq \left(\sum_{j=1}^{n} x_i \right)^2 \left(\sum_{j=1}^{n} y_i \right)^2 \text{ for } x_i, y_i \in \mathbb{R} \tag{3.8}$$

and applying this inequality to the sums on the right-hand-side of equation (3.7), we see that

$$\sum_{i,j,k=1}^{3}\left(\frac{\partial\varphi}{\partial x_k}\right)^2\left(\frac{\partial^2\varphi}{\partial x_i\partial x_j}\right)^2 \geq \sum_{i,j,k=1}^{3}\left(\frac{\partial\varphi}{\partial x_i}\right)\left(\frac{\partial\varphi}{\partial x_k}\right)\left(\frac{\partial^2\varphi}{\partial x_i\partial x_j}\right)\left(\frac{\partial^2\varphi}{\partial x_k\partial x_j}\right) \tag{3.9}$$

From this it follows that the sign of μ_{eff} determines the sign of $\vec{\nabla}\cdot\vec{F}$. Consequently, equation (3.3) is fulfilled for molecules in quantum states with $\mu_{eff} < 0$, i.e. for low-field-seeking (LFS) states. For molecules in LFS, the Stark energy increases with the increase in an electric field, resulting in a force towards the regions of lower field. For such molecules the focusing can be readily achieved using static electric fields since the electric field minima in free space is eminently realizable. For high-field-seeking (HFS) states the energy decreases with the increase in the electric field and $\mu_{eff} > 0$. Maxwell's equations do not allow for an electric field maximum in a charge-free space, therefore, when dealing with HFS states one finds that the molecules have a tendency to crash into electrodes. This makes it impossible to focus or trap molecules in HFS states using static electric fields alone. This is analogous to the case of charged particles where for a particle of charge q, the divergence of the force field is $\vec{\nabla}\cdot\vec{F} = q\vec{\nabla}\cdot\vec{E}$ and since in charge-free space $\vec{\nabla}\cdot\vec{E} = 0$, therefore $\vec{\nabla}\cdot\vec{F} = 0$. Both molecules in HFS states and charged particles do not satisfy the necessary condition for confinement, Equation 3.3. Nonetheless, focusing and trapping can still be achieved if dynamic focusing fields are utilized.

In 1949 Nicholas Christofilos [58], a Greek physicist, invented and, subsequently, patented a dynamic focusing method for charged particles that is now commonly known as "alternating-gradient" focusing. Since 1950s the method has been analyt-

ically refined and successfully implemented in charged-particle accelerators [61]. In mid 1960s, the same method was proposed for the case of neutral particles [59] and was experimentally demonstrated by Kakati and Lainé [62] for the transverse focusing of ammonia molecules in HFS quantum states. The basic idea, in turn, is borrowed from optics where it was shown that appropriately spaced focusing and defocusing lenses will result in a net focusing of the light rays. In accelerator physics, the glass lenses are replaced by electrostatic lenses that focus the particles along one transverse direction while defocusing along the orthogonal transverse axis. Alternating the orientation of these lenses (or the fields produced by them) at an appropriate frequency results in a net transverse focusing of the particle beam. Particles moving away from the beam axis experience an increasing force towards or away from the beam axis depending on the type of the lens used. In linear optical systems the force is directly proportional to the excursion distance from the beam axis. After going through the focusing lens the particles are positioned closer to the beam axis when entering the defocusing lens and hence, on average, experience a weaker defocusing force and a stronger focusing force. The idea can be extended to confine particles in three dimensions as is done in Paul traps [63]. A notable difference between charged particles and neutral (polar) molecules is that for the latter, the value of the effective dipole moment μ_{eff} is quantum-state dependent and may not necessarily be constant in an inhomogeneous electric field, as assumed above.

3.2 Electrode Geometries

In this section, we discuss how a suitable electrode geometry may be constructed for efficient AG focusing. First, an analytically treatable approach will be presented based on a multipole field expansion. Then we present numerical studies of elec-

trode geometries that approximate the ideal geometries but are constrained to be in consonance with readily achievable, modern micro- and nanolithographic methods.

For the analysis that follows and for the remainder of the thesis we will assume that the molecular dipole moment is constant. In the limit of strong electric fields and for small changes of the fields, the effective dipole moment may indeed be approximated as constant [54] with the Stark shift that is linearly proportional to the applied electric field. To achieve optimum optical properties in a lens a linear focusing is needed [64]. This would result in an aberration-free lens with molecules experiencing a harmonic interaction potential in the transverse plane. In the case of a linear Stark shift, with constant effective dipole moment, and a harmonic interaction potential in the transverse plane, the ideal form for the strength of the electric field is also harmonic: $E(x, y) = E_0 + \eta(x^2 - y^2)$. Such a lens would focus molecules in one transverse direction and defocus them in the orthogonal direction. Although such a field cannot be realized, it is nonetheless possible to construct a field that is a good approximation to the ideal one. Deviations from the ideal, especially when strong nonlinearities are present, will result in a partial beam loss, generation of beam halo and larger beam sizes. Such deviations, however, are not as critical for the purposes of loading traps and subsequent manipulation of qubits.

Following the proposed method taken by *Kalnins et al.,* in reference [64] and *Bethlem et al.,* in reference [61] we analyze the electric field from the electrodes with the use of a multipole field expansion.

The most general form of a 2D electrostatic potential φ, that is consistent with the Laplace's equation, may be represented by a multipole expansion as:

$$\varphi(r,\theta) = \varphi_0 \left[\sum_{n=1}^{\infty} \frac{a_n}{n} \left(\frac{r}{r_0} \right)^2 \cos(n\theta) + \sum_{n=1}^{\infty} \frac{b_n}{n} \left(\frac{r}{r_0} \right)^2 \sin(n\theta) \right] \tag{3.10}$$

where, $r = \sqrt{x^2 + y^2}$ and $\theta = \arctan(\frac{y}{x})$ are the usual cylindrical coördinates. a_n and b_n are the dimensionless constants while r_0 and φ_0 are the scaling factors that characterize the length scale for the chosen electrode geometry and the applied voltages, respectively. The $n = 1$ terms in equation (3.10) represent a constant electric field while $n = 2$ and $n = 3$ terms represent the familiar quadrupole and hexapole fields used extensively in guiding of the molecules in the LFS states [65]. The magnitude of the electric field E_0 on the molecular beam axis is related to φ_0 by $E_0 = (\frac{\varphi_0}{r_0})\sqrt{a_1^2 + b_1^2}$.

To obtain a maximum of the electric field along one transverse direction and a minimum along an orthogonal transverse direction, a nonzero magnitude of the electric field along the beam axis is needed. Furthermore, the electric field strength should be symmetric under the reflection on the x- and y-axis. Consequently, the electrostatic potential should be symmetric under the reflection along the x-axis and antisymmetric under the reflection along the y-axis. This can be achieved by setting all $b_n = 0$ and retaining only the odd a_n terms in equation (3.10). Since higher-order terms introduce nonlinearities in the focusing force, resulting in undesired aberrations, only terms up to $n = 5$ are used.

Then multipole expansion in Cartesian coördinates ($x = r\cos\theta$ and $y = r\sin\theta$) becomes:

$$\varphi(x,y) = \varphi_0\left(a_1\frac{x}{r_0} + a_3\frac{x^3 - 3xy^2}{r_0^3} + a_5\frac{x^5 - 10x^3y^2 + 5xy^4}{5r_0^5}\right) \tag{3.11}$$

The magnitude of the electric field may be calculated from $\varphi(x,y)$:

$$E(x,y) = \sqrt{\left(\frac{\partial\varphi}{\partial x}\right)^2 + \left(\frac{\partial\varphi}{\partial y}\right)^2} \tag{3.12}$$

Assuming small deviations from the molecular beam axis ($r < r_0$) and that $a_1 \gg a_3 \gg a_5$, the electric field can be expanded as a power series:

$$E(x,y) = E_0\left(1 + \frac{a_3}{a_1}\frac{(x^2 - y^2)}{r_0^2} + 2\left(\left(\frac{a_3}{a_1}\right)^2 - 3\frac{a_5}{a_3}\right)\frac{x^2y^2}{r_0^4} + \frac{a_5}{a_3}\frac{(x^4 + y^4)}{r_0^4} + \cdots\right) \tag{3.13}$$

From this we see that the harmonic term, second term in the expansion, scales as a_3/a_1 while the three anharmonic terms scale as $(a_3/a_1)^2$ and a_5/a_3, respectively. Thus, to produce the desired focusing potential, the electrode geometry must be chosen that minimizes a_5 while keeping a_3 large enough to produce sufficient focusing and yet small enough to reduce undesired aberration effects.

Controlled loading of traps, for quantum information processing purposes, does not require significant throughput since there are more than enough molecules even in a very poor molecular beam to load dozens of trap sites. Hence, unlike in molecular

beams for crossbeam collision studies where number of molecules is important, for our purposes even significant deviations from the ideal field are tolerable. It should be kept in mind that the harmonicity of the electric field, discussed above, is based on the assumption that the effective dipole moment is constant and therefore, does not depend on the electric field itself.

The two electrode geometries selected for this work are a compromise between those that produce transverse harmonic fields, those that producing significant longitudinal (on-axis) electric fields for deceleration or acceleration and those that are possible to make with common micro- and nanolithographic methods. In order to achieve focusing, the gradient of the electric field has to be rotated 90 degrees at some distance ahead. This can be accomplished in two different ways, corresponding to the two chosen geometries, either by rotating the electrodes 90 degrees (z-shape geometry) or by changing the applied voltage polarity (RFQ-type geometry). In the following sections we analyze the resultant fields. This work is part of an on-going experiment of which the next step is to perform trajectory simulations and to analyze the molecular motion.

3.2.1 Z-shaped

The z-shaped electrode geometry is, in essence, a combination of the two-rod alternating-gradient type structure for transverse focusing (due to the rods located at the corners of the simulation cell, referred to as the guiding segments) and a typical two-rod Stark decelerator type structure for affecting the longitudinal motion (due to the two parallel rods in the middle of the simulation cell, referred to as the central segments). Figure 9 depicts a simulation cell used in CoMP2 program containing z-shaped electrodes and, effectively, representing one stage of our device.

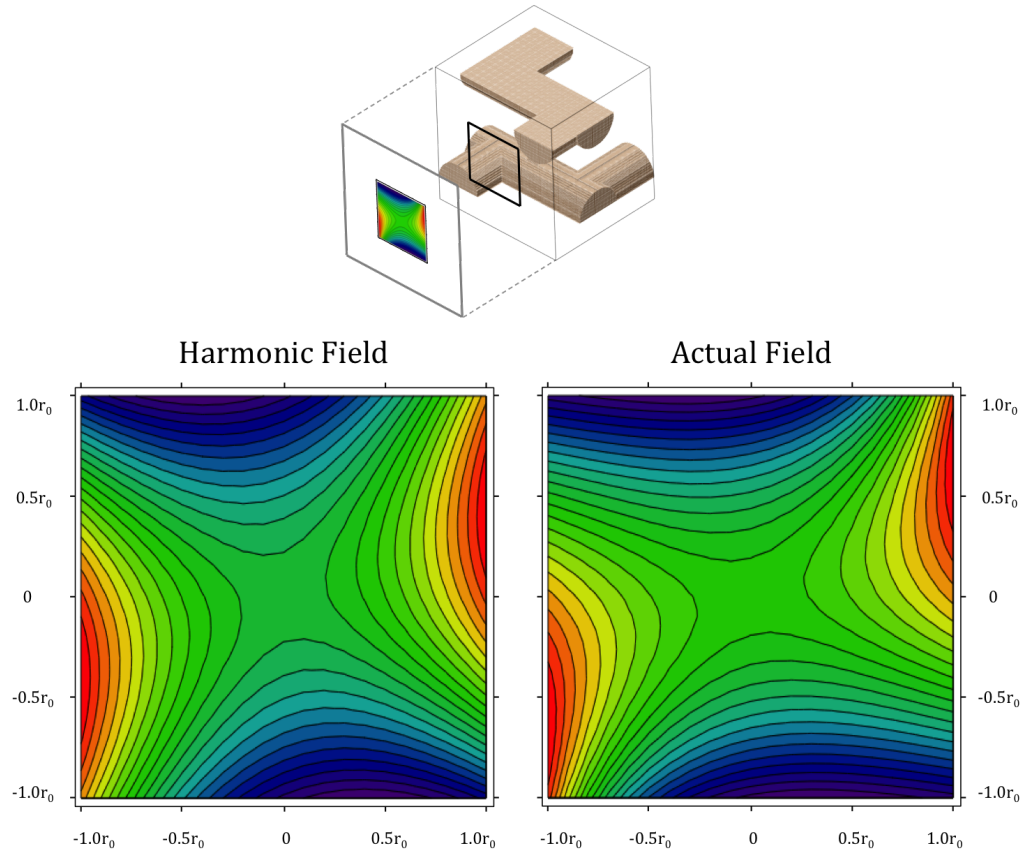

Figure 9. Comparison of the Transverse Electric Field from the Z-shaped Geometry with a Purely Harmonic Field. We obtain the transverse electric field from the z-shaped geometry along the plane perpendicular to the beam axis and a distance of $2R$ away from the center of the stage. This field is then compared to the purely harmonic field. Red color designates regions of high electric field.

A time-dependent voltage of opposite polarity is applied to the top and bottom electrodes. Note that the time-dependence of the applied voltage is only necessary in order to decelerate or accelerate the molecules but not for transverse focusing. Applying a constant, time-independent, voltage to the electrodes as the molecules fly through the device should keep molecules transversely focused by virtue of alternating focusing/defocusing electrode structures.

To analyze the transverse component of the electric field we map its magnitude everywhere on the plane perpendicular to the beam axis (z-axis) and located at a distance of $2R$ away from the center of the stage, see Figure 9. This distance was intentionally chosen to be very close to the central electrode segments (stretching along the x-axis). Moving further away from the center of the stage we expect the electric field to approach that of the typical two-rod AG scenario with $a_3/a_1 = \pm 1/7$. Deviations from this can be attributed to the presence of the central electrode segments. Thus, taking measurements at a distance of $2R$ away from the x-y plane going through origin will provide us with an estimate of the 'worst case' scenario.

Also shown is a comparison of the pure harmonic field ($E_0 = 43$ kV/cm and $\eta = 0.24$) with the actual electric field which has $a_3/a_1 = 0.349$. The ratio a_3/a_1 determines the strength of the anharmonic term and we see that it is almost double that of the ideal field. Two things to note: first, the presence of the central electrode segments stretches the field near the center predominantly in the x direction, thereby reducing the field gradient (force) everywhere along the x-axis. This makes this particular configuration weaker at focusing the molecules along the x-axis. The field gradient along the y-axis however, has increased. Second, these field distortions imply that $a_5 > 0$ which will result in noticeable aberration effects. Nonetheless, our preliminary testing shows that it is possible to reduce these distortions significantly by changing the separation distance between the upper and lower guiding electrodes. The effect of asymmetric electrodes (i.e. the upper and lower guiding electrodes having different radii) on the shape of the electric field should be examined.

As was mentioned earlier, it is important to consider not only the shape of the electric field but also its magnitude. Ideally, one would want to have high field

gradients and large variation in the electric field magnitude for maximum control over the molecular motion and higher overall transmission. The transverse velocity distribution, in a typical molecular beam experiment, is centered on 0 m/s with a full-width-at-half-maximum (FWHM) spread of a few tens of m/s. Such molecular spreads can be completely focused with fields around 100 kV/cm. While the longitudinal velocity distribution is less determined because it depends on the regime of the gas expansion (see, Section 4.1 and Section 4.1). Forward speeds between 200 - 600 m/s are expected when using either the supersonic or the buffer gas techniques therefore, if the molecule experiences a Stark shift on the order of 1 cm^{-1} within each stage then the molecules could be decelerated to a standstill within 100-200 stages.

Molecules flying along z-axis encounter a pair of guiding electrode segments at the beginning and at the end of each stage, see Figure 10. The electric field produced by the first pair is identical to the electric field produced the next pair except that it is rotated by 90 degrees. Therefore, due to electrode symmetry, the electric field strength and the gradient along the solid blue-axis between the lower (solid, grey) and upper (solid, orange) electrode segments will be identical to the one along the solid green-axis between the upper and lower electrodes at the end of the stage. Consequently, we need only to look at the electric field and its gradients for one pair of the guiding segments. In this geometry, molecules in high-field-seeking states will be defocused in the plane containing the electrode centers (solid, blue-axis) and focused in the orthogonal plane whereas molecules in the low-field-seeking states will do the opposite.

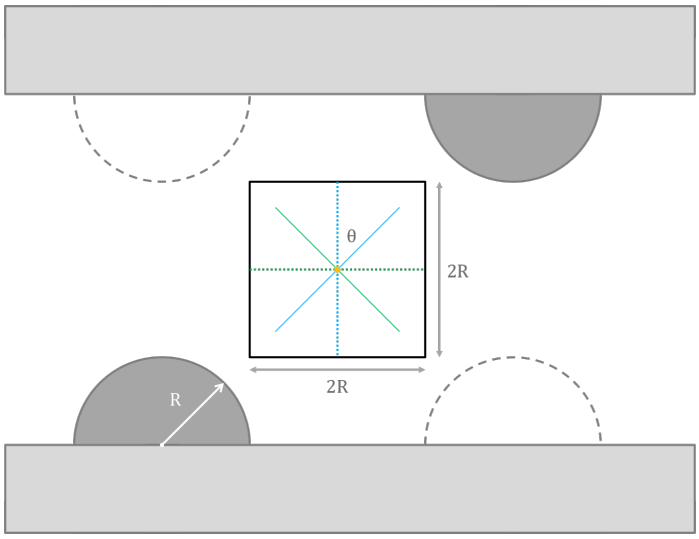

Figure 10. Diagram of the Guiding Electrode Segments in the Z-shaped Geometry. The molecules fly along the z-axis (into the page) and encounter the first pair of guiding electrode segments (solid). After passing the central electrode segments the molecules are guided by another set of electrode segments (dashed), which rotate the resultant field by 90 degrees. The substrate, on which the electrodes are deposited, is shown in grey.

For efficient AG guiding it is best if the strength of the defocusing force, which is proportional to the gradient of the field, equals that of the focusing force and that these forces are linear. In practice, it is hard to get rid of the nonlinearities and consequently, forces are only approximately linear near the beam axis, becoming less linear, for example, as we move closer to the electrodes. Figure 11 shows the variation in the field magnitude and its gradients for the guiding segments (a-b) and for the central segments (c-d) responsible, primarily, for deceleration/acceleration. All electrodes in this z-shaped geometry have radius $R = 2.5\mu$m. Opposing electrode segments have an approximate center-to-center distance of $4\sqrt{2}R$. A voltage of ± 20 V was applied to the upper and lower electrodes, which are separated by a distance of $2R$. The magnitude of the electric field along the beam axis for the guiding segments

is around 43 kV/cm (Figure 11a), which of course is lower than that of the central segment where the magnitude is 72 kV/cm due to the central segments having smaller center-to-center separation distance.

There is a 12% - 20% magnitude variation between the field at a distance of R and the field along the beam axis, which is large enough to transversely confine most of the molecules within a typical molecular beam. The field gradients (Figure 11b) along the blue and green axes are not equal however, with the gradient along the blue axis being the largest. By looking at the graph we see that that the gradients are only linear within a distance of $\pm 0.5R$. All these parameters are close to or better than those of the macroscopic AG decelerators already in use [66][67][68]. Ideally the central segments would only provide decelerating/accelerating fields and gradients Figure 11c-d (in orange). While there is almost no gradient along the x-axis there is nonetheless, an unavoidable large gradient along the y-axis. This means that during deceleration (acceleration) the molecules will experience changing transverse fields that may negatively impact the total transmission. However, just by looking at the shape and gradients of the field it is hard to predict to what extent the presence of the central segments will distort the molecular motion. In the end, full 3-dimensional trajectory calculations need to be carried out to determine the details of the molecular motion inside the z-shaped electrode geometry.

In this analysis we have not considered the effects that the presence of a particular substrate would have on the electric field and any of the resulting transient fields. Of course, before building the actual microchip the presence of the substrate would need to be properly accounted for.

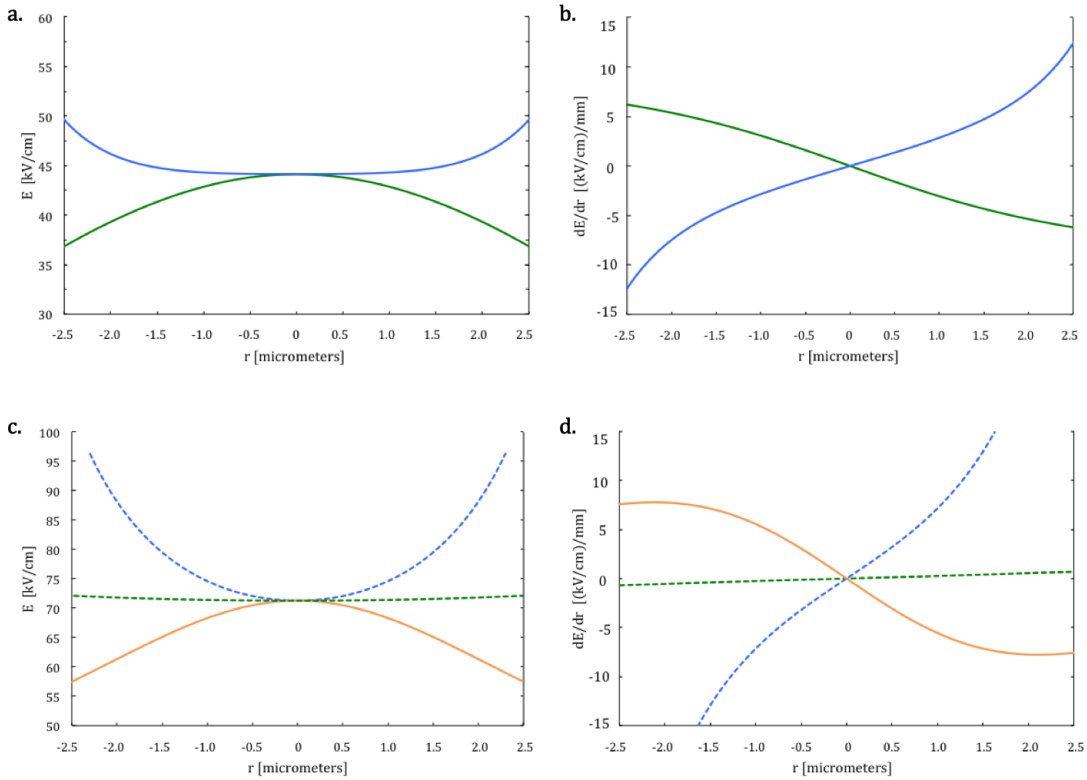

Figure 11. Plots of the Electric Field Magnitudes and the Corresponding Gradients for the Guiding Electrode Segments and for the Central Segments in the Z-shape Geometry. The electric field magnitudes are plotted in (a & c) and the corresponding gradients are plotted in (b & d) for the guiding electrode segments (a-b) and for the central segments (c-d) according to the color and line-type scheme of Figure 10.

There still remains a question of tiling. That is, thus far we have only worked with a unit cell of the z-shaped geometry but the envisioned microchip will consist of many cells joined together on a substrate covering an area of approximately 2 cm x 2 cm. Figure 12 shows two of the possible ways that such a geometry may be tiled on a surface. A special attention must be paid to the placement of the electrode pads, supplying the voltage to the electrodes, as they will likely be a major source of field distortions near the edges of the microchip.

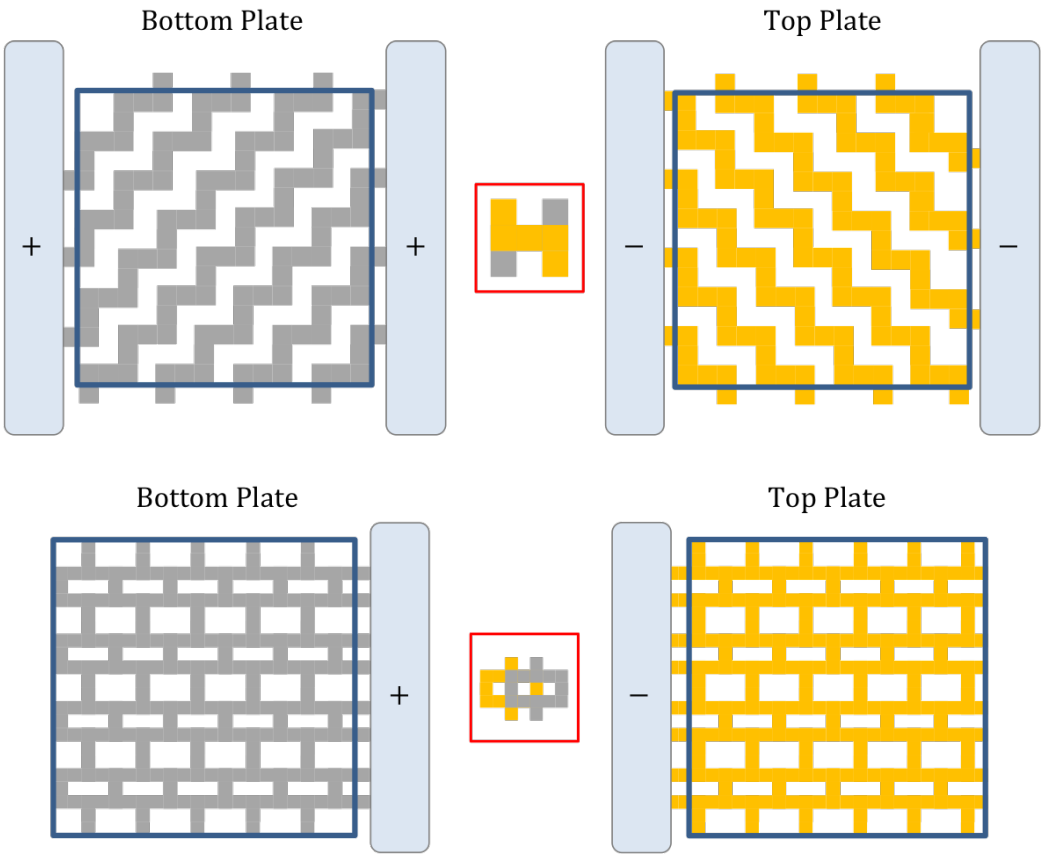

Figure 12. Two Possible Ways of Tiling a Surface with the Z-shaped Electrodes. In its basic form the microchip will consist of two parallel plates containing electrodes and electrode pads (light blue), which supply voltage to the electrodes. The unit cells containing both the top (yellow) and bottom (grey) electrodes are shown in the middle.

The "double-phi" tiling is better than a straightforward "double-z" tiling for two reasons. First, it can manipulate a greater number of molecules since in the double-z arrangement there are wasted channels (the field switching period will be out of synch with the placement of the electrodes for some of channels). Second, only two electrode pads are needed which could be placed on opposite sides of the microchip in order to minimize noise.

3.2.2 RFQ-type

Typically, low-field-seekers are guided with the use of quadrupole and hexapole electrode arrangements that maintain an electric field minima along the axis of propagation. These guides are, in essence, four or six very long cylindrical electrodes of radius $R = const.$ If the long electrodes are slightly bent then one can select molecules in LFS states that have certain maximum velocity out of the molecular beam containing both HFS and LFS states. These devices are termed "selectors" for obvious reasons. Such schemes cannot be used for guiding or selecting molecules in HFS states, as the molecules will crash into the electrodes where the electric field is always the strongest. The AG principles, however, can be applied to the quadrupole and hexapole electrode arrangements as well, making it possible to guide molecules in LFS and HFS states. In the symmetric electrode configurations the alternation of the electric field gradient is achieved by changing polarities of the applied voltages thereby interchanging focusing and defocusing planes.

Such an arrangement cannot be used to accelerate or decelerate molecules either, as there is no longitudinal gradient. This is solved by modulating the distance between the electrodes, thereby, producing the necessary longitudinal acceleration component. For example, in a four-rod (quadrupole) arrangement the modulation can be achieved by bending the electrodes towards or away from the beam axis or by continuously changing the diameter of the electrodes as a function of the longitudinal position, such that $R = R(z)$. Yet another way is to coat the metallic electrodes with a dielectric such that the thickness of the dielectric is a function of the longitudinal position. In either case, if the periodicity of these modulations is matched to the synchronous

particle's path, then it becomes possible to accelerate molecules in a phase-stable manner.

Our electrode geometry is shown in Figure 13. It is loosely based on the electrode geometry typically seen in a Radio-Frequency Quadrupole (RFQ) that bunches, focuses and accelerates lower energy protons and ions using only RF fields [69]. Unlike other linear accelerators, which use discrete segments for acceleration and focusing (for example, Alvarez-type accelerator), RFQ performs its functions using space-uniform alternating gradient structures. Two common types of the electrode geometries used in RFQ can be seen in Figure 14. What makes RFQ different is that it is fundamentally a transverse focusing device with longitudinal acceleration added as a perturbation via the modulating electrode-surface function. The operational principles of RFQ can also be extended to the case of polar molecules.

We want to see what effect the sinusoidal modulations, in our four-rod electrode arrangement, have on the resultant longitudinal inhomogeneity and to also study transverse fields and gradients. Although here we use electrodes with rectangular cross section, this is not an essential feature and typical cylindrical electrodes or electrodes with semicircular cross section may be used instead. The same labeling convention is used as in the original RFQ. The surfaces of the otherwise flat electrodes is modulated with a sinusoidal function such that the minimum separation distance between neighboring electrodes remains constant (i.e. $a = 2.5\mu$m), while the amplitude of the function is varied (2.5 μm, 1.5 μm, 0.5 μm). The modulation is restricted to x-z plane only. As before, we measure the electric field and the gradient.

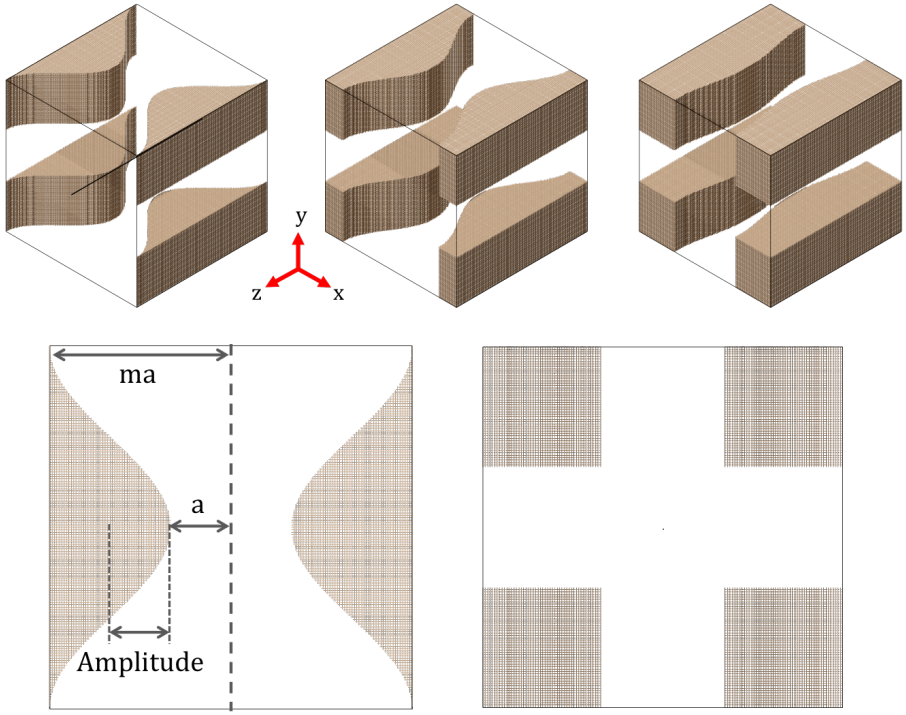

Figure 13. RFQ-type Electrode Geometry for Accelerating Polar Molecules. The top panel shows three simulation cells with different amplitudes (2.5 μm, 1.5 μm, 0.5 μm) of the sinusoidal modulations with $a = 2.5\mu$m. The bottom panel shows slice of the x-z plane and x-y plane. The molecular beam axis runs through the middle of the simulation cell in the z-direction.

In the transverse direction the measurements are taken on the plane through the middle of the simulation cell while the longitudinal field is monitored along the beam axis, see Figure 15.

The results are displayed in Figure 16. Increasing the amplitude of the modulating function decreases the value of the electric field on the beam axis from 54.5 kV/cm for amplitude of 0.5 μm to 50 kV/cm for amplitude of 2.5 μm. This is a small decrease in the electric field magnitude for a rather large variation in the amplitude.

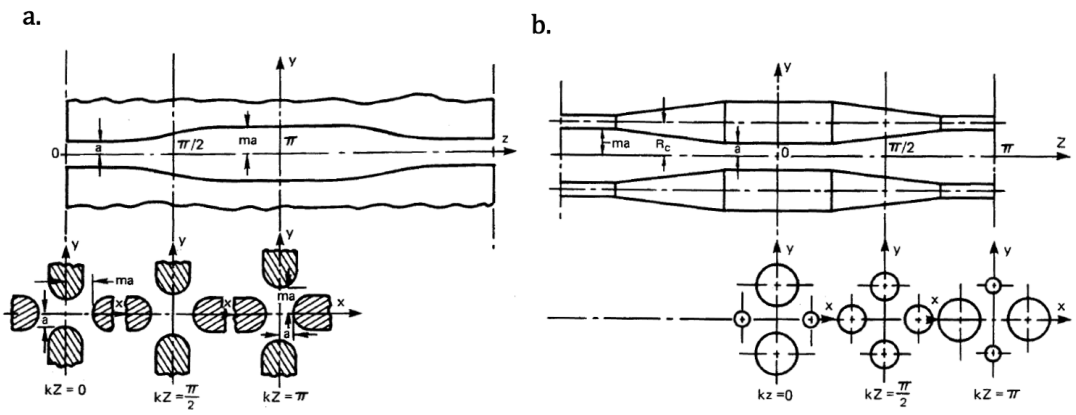

Figure 14. Two Common Types of RFQ Electrode Geometries. (a) Semicircular electrodes with sinusoidal transitions and (b) cylindrical variable-diameter electrodes with conical transitions. Reproduced from Reference [70].

More important are the values of the electric field everywhere along the beam axis, since these fields are responsible for deceleration and acceleration of molecules. We see that, while all three geometries produce some inhomogeneity along the beam axis, the largest inhomogeneity is produced by the geometry with the largest amplitude. This implies that using geometry with 2.5 μm amplitude would allow one to use fewer stages to decelerate a molecule to a standstill. It has both the largest difference between the minimum and maximum values of the electric field and produces the strongest longitudinal forces. Furthermore, it also compares well in regard to the transverse fields. Although the gradients along the y-axis (blue) are slightly weaker for this geometry, they are more symmetric and almost equal to the gradients along the x-axis (green) that would result in a better AG focusing. All three geometries produce relatively linear forces, close to the beam axis. These forces are stronger than the corresponding transverse forces in the z-shaped geometry.

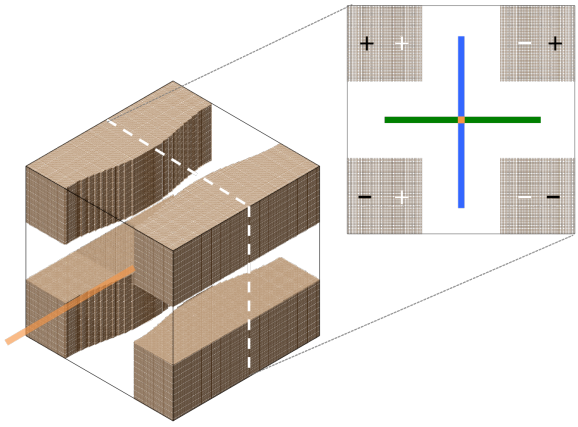

Figure 15. RFQ-type Simulation Cell for Polar Molecules. The transverse fields and gradients are examined along x-y plane through the middle of the simulation cell (insert) while the longitudinal field is monitored along the beam axis (colored green). Alternation in the field gradient is achieved by switching the applied voltage from configuration 1 (black) to configuration 2 (white).

From this analysis one can conclude that the geometry with a 2.5 μm amplitude of the sinusoidal modulating function is the best candidate having, not only the strongest longitudinal forces, but also a more favorable transverse electric field distribution. Although the transverse forces in this geometry are better than those of the z-shaped geometry, the longitudinal forces are actually weaker, see Figure 16d. This is due to the electrodes being further apart in this electrode arrangement than in the z-shaped one.

To achieve alternation in the gradient, the applied voltage is switched from configuration 1 to configuration 2, see Figure 15. Due to asymmetry in the electrode geometry, the rotated electric field distribution is only approximately equal to that in configuration 1. However, as was mentioned above, one can create modulation function that is not only a function of z but is also radially symmetric.

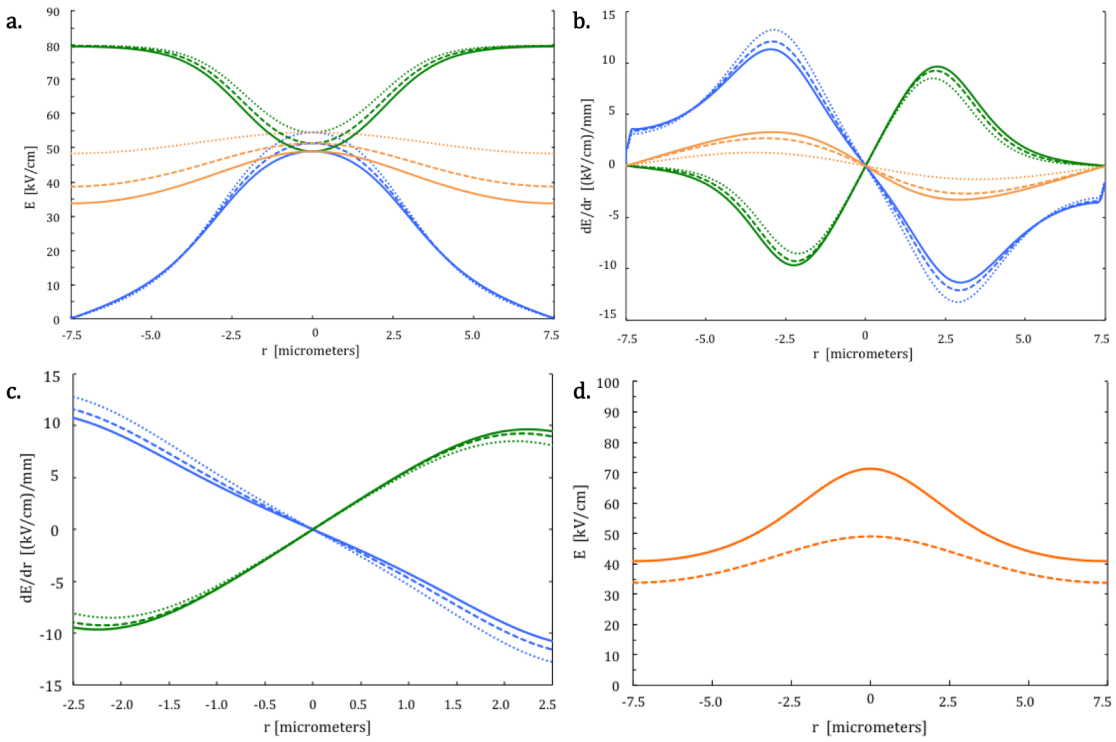

Figure 16. Plots of the Electric Field Magnitudes and Gradients for the RFQ-type Geometry with Different Amplitudes of the Modulating Function. The electric field magnitudes are plotted in (a & d) and gradients are plotted in (b & c) in RFQ-type electrode geometry with three amplitudes of the modulating function: 0.5 μm (dotted line), 1.5 μm (dashed line) and 2.5 μm (solid line).

It should be noted that the electrode structures and configurations used in charged-particle RFQs cannot be directly applied to the case of polar molecules due to the differences in the way that a charged particle and a dipole couple to the electric field. As a concrete example, we can use the typical RFQ electrode configuration where the electrodes on one diagonal are out of phase with the electrodes on the other diagonal, see Figure 17a.

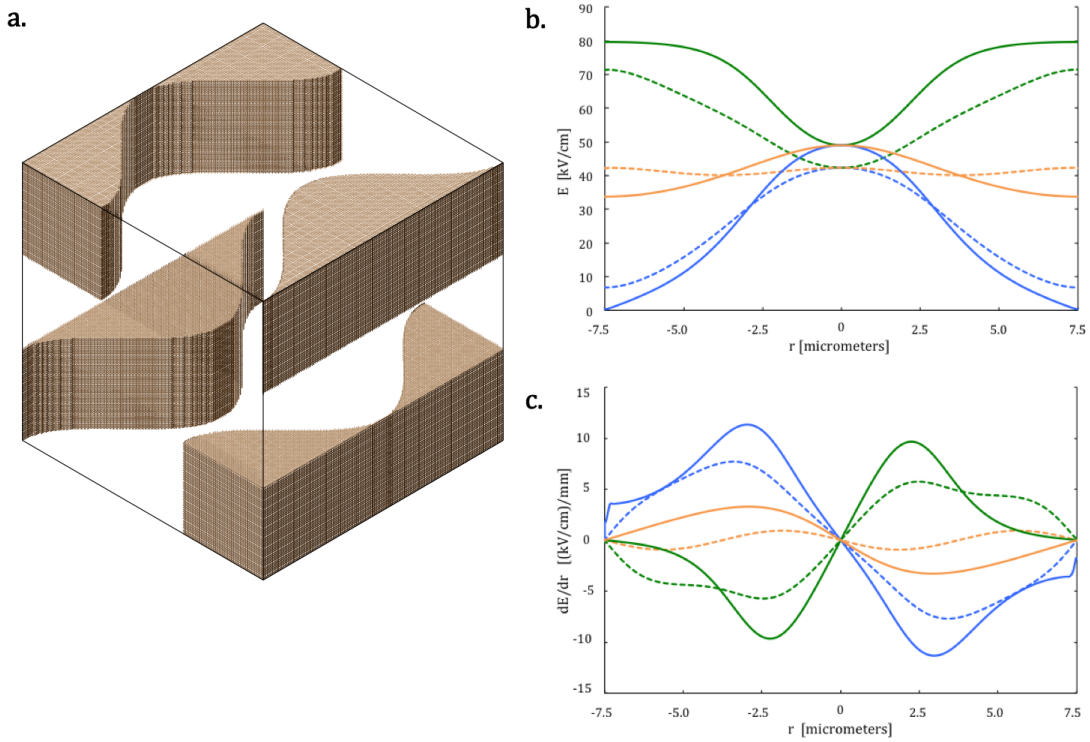

Figure 17. Comparison of 'in Phase' and 'out of Phase' RFQ-type Electrode Structures. (a) Typical electrode arrangement in a charged-particle RFQ. Compared are both (b) electric field magnitudes and (c) gradients of this electrode arrangement (dashed lines) with our RFQ-type electrode geometry (with 2.5 μm amplitude modulating function), which has all electrodes 'in-phase' (solid lines).

Comparing this configuration with our best candidate geometry from above, we see that our RFQ-type electrode geometry, where all four electrodes are in-phase with each other, is better than the typical charged-particle RFQ arrangement, see Figure 17b-c. Our RFQ-type geometry results in stronger fields, stronger forces and a substantially better longitudinal electric field distribution. From a practical point of view, the resultant electric field inhomogeneity from a typical RFQ arrangement is so small that it cannot be used for deceleration or acceleration of polar molecules.

3.3 Transverse Equations of Motion

In this section, the transverse motion of molecules in an alternating gradient scenario is briefly analyzed. We restrict the treatment to a simple case of harmonic interaction potential and a constant (field independent) effective dipole moment. Also, for simplicity, the transverse and longitudinal motions are assumed to be independent (decoupled).

Due to the assumption that the interaction potential is harmonic, close to the beam axis, the molecule experiences a linear focusing force in one direction and a linear defocusing force in a perpendicular direction. The electric field near the beam axis is also harmonic of the form $E(x,y) = E_0 + \eta(y^2 - x^2)$ with the interaction potential given by $W(x,y) = -\mu_{eff}(E_0 + \eta(y^2 - x^2))$. For HFS molecules and $\eta > 0$ this interaction potential results in focusing along the x-axis and defocusing along the y-axis. By comparison with Equation 3.13 and, by neglecting higher-order terms, we see that $\eta = \dfrac{(E_0 a_3)}{(a_1 r_0^2)}$. Using this form of the interaction potential, the equation of motion along the beam axis can be written as

$$m\ddot{x} = \mp 2\mu_{eff}\eta x \tag{3.14}$$

which leads to,

$$\ddot{x} \pm \frac{2\mu_{eff}\eta}{m}x = 0 \tag{3.15}$$

The plus and minus signs correspond to the focusing and defocusing forces, respectively. The angular oscillation frequency, Ω, is

$$\Omega = \sqrt{\frac{2\mu_{eff}\eta}{m}} = \sqrt{\frac{2\mu_{eff}}{m}\frac{E_0 a_3}{a_1 r_0^2}} \tag{3.16}$$

The equation of motion can be recast into a more useful form if we assume that the molecule moves with a constant forward speed v_z. Thus,

$$\frac{\partial^2 x}{\partial t^2} \pm \kappa^2 v_z^2 x = 0 \tag{3.17}$$

Written in terms of the variable z, we have

$$\frac{\partial^2 x}{\partial z^2} \pm \kappa^2 x = 0 \tag{3.18}$$

with $\kappa/2\pi$ describing the number of oscillations per unit length, and where

$$\kappa = \sqrt{\frac{2\mu_{eff}\eta}{m v_z^2}} = \frac{\Omega}{v_z} \tag{3.19}$$

The equation of motion, Equation 3.18, takes the form of Hill's differential equation. Assuming $v_z = const$ enables us to solve Hill's equation analytically. It should be noted that this assumption of a constant forward speed is not a strict one and it relates to the type of the waveform applied to the electrodes. What needs to be true is that the forward speed can be approximated to be constant over some finite intervals.

In other words, Hill's equation can be solved analytically if the period of the arbitrary periodic waveform applied to the electrodes can be divided into a finite number of intervals of constant voltage [71]. This corresponds to a special case of a piecewise constant waveform. General matrix method for calculating solutions of Hill's differential equation have been developed [71] and successfully used in charged particle physics [72].

Since Equation 3.18 is a second order linear differential equation, the solution is uniquely determined by the initial conditions and can be written as [54]

$$\begin{pmatrix} x(z) \\ v_x(z) \end{pmatrix} = M(z|z_0) \begin{pmatrix} x(z_0) \\ v_x(z_0) \end{pmatrix} \tag{3.20}$$

where $M(z|z_0)$ is the transfer matrix given by

$$M(z|z_0) = \begin{cases} \begin{pmatrix} \cos(\kappa l) & \frac{1}{\Omega}\sin(\kappa l) \\ -\Omega\sin(\kappa l) & \cos(\kappa l) \end{pmatrix} & \text{F : focusing region} \\ \begin{pmatrix} 1 & \frac{l}{v_z} \\ 0 & 1 \end{pmatrix} & \text{O : drift region} \\ \begin{pmatrix} \cosh(\kappa l) & \frac{1}{\Omega}\sinh(\kappa l) \\ \Omega\sinh(\kappa l) & \cosh(\kappa l) \end{pmatrix} & \text{D : defocusing region} \end{cases} \tag{3.21}$$

with $l = z - z_0$. Transfer matrices F, O or D are used depending on the situation. For example, in a z-shaped geometry discussed earlier, the molecule would experience

focusing for some length L_1 while approaching the central segments and therefore F transfer matrix would be used. Then the field is turned OFF for some period of time during which the molecule drifts at a constant speed, for some length S, and therefore O matrix is used. When the field is turned back ON, the molecule experiences a rotated field, which causes defocusing, for some length L_2, and therefore D matrix is used in that region. Then the field is turned OFF again and the process repeats. Finally, the AG array can be written as $F(L_1) \cdot O(S) \cdot D(L_2) \cdot O(S)$. If the whole device is composed of n such arrays then the transfer matrix for the whole device can be expressed as $M = (FODO)^n$. The molecular trajectories will remain stable if all the elements of the transfer matrix remain bounded as n tends to infinity, which is true for $-1 < \frac{1}{2}Tr(M) < 1$.

Using Courant-Snyder parameterization of the transfer matrix, we can write down the solution to Equation 3.18 describing the trajectory of the molecule moving through an AG array as

$$x(z) = \sqrt{\beta(z)\epsilon_i}\cos(\phi(z) + \delta_i) \tag{3.22}$$

where ϵ_i and δ_i are the parameters defining the initial conditions of the particular molecule, $\beta(z)$ is the Courant-Snyder parameter and $\phi(z) = 1/v_z \int_0^z 1/\beta(z\prime)dz\prime$ is the z-dependent phase. The general motion of the particle is comprised of a micromotion superimposed on a macromotion, similar to the motion of ions in Paul traps [63].

3.4 Alternating-Phase Focusing (APF)

A radio-frequency quadrupole (RFQ) system is capable of affecting particles longitudinal and transverse motion using only RF fields. This has both operational and

constructional advantages. Around the same time as the invention of RFQ in the 1960's, a very different method was proposed to accomplish the same task as RFQ. In the accelerator physics community this method came to be known as the alternating phase focusing (APF) method that was first proposed by M.L Good [73] and Ya. B Faynberg [74]. Accelerators implementing APF can simultaneously accelerate and focus charged particle beams with only the accelerating field itself providing radial as well as longitudinal beam stability. By periodically changing the polarity and magnitude of the synchronization phase, a charged particle may be stably accelerated [75]. Unlike RFQ, APF is much less known and we found no reference to this method in the molecular beam community. Nonetheless, this method seems promising even in regard to polar molecules. It may prove to be particularly useful in the context of microchips where the geometry is typically two-dimensional (2D planar), thus making it hard to integrate focusing elements in addition to accelerating-decelerating structures while keeping construction simple.

In a linear accelerator the need for external transverse focusing elements, such as quadrupoles, is motivated by the fact that the synchronous phase is chosen in the rising part of RF voltage waveform to ensure longitudinal bunching, but at the same time inducing transverse defocusing. A similar situation arises when working with polar molecules. To see this, we look at the evolution of the potential energy surface produced by a two-dimensional lens made up of two electrode pairs as shown in Figure 18. The lens can be assumed to extend to infinity in the z-direction, that is, we neglect the edge effects. We look at how the longitudinal (y-axis) and transverse (x-axis) curvatures of the potential energy surface change when we vary the voltage applied to one of the electrode pairs.

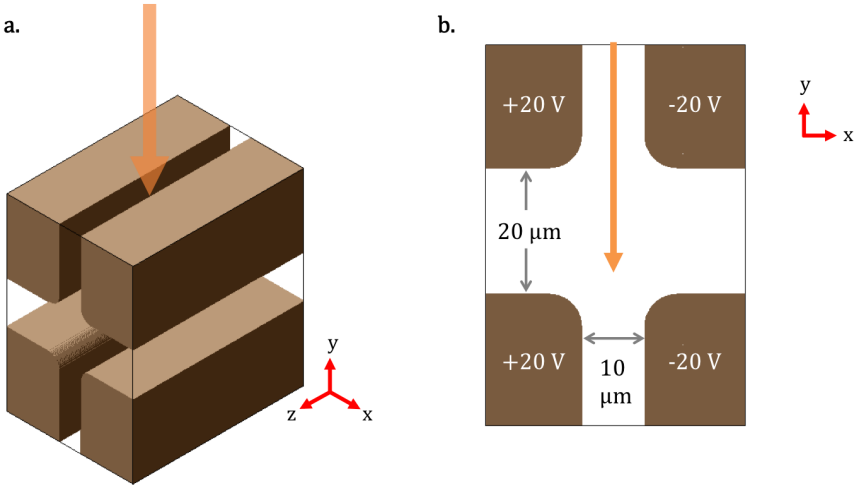

Figure 18. 3D Simulation Cell and x-y Plane Slice of a Lens Used in APF Study. (a) 3D simulation cell and (b) x-y plane slice of a lens used in APF study. The path of the molecular beam is shown as an orange arrow. The edges of the electrodes, comprising the lens, are rounded with a quarter-circle of radius 5 μm. The lens actually extends much further along the z-axis. We only look at the fields in the middle of this long lens, which enables us to neglect the edge effects.

Looking at Figure 19, we see that when the potential difference of the left electrode pairs is kept at 40 V, while the right pair of electrodes is grounded, then the potential energy hill is convex everywhere. This would cause transverse defocusing resulting in molecules slamming into the electrodes. However, as the potential difference of the right electrode pair is increased we see the top portion of the hill becoming concave, i.e. transverse focusing. We note that the bottom portion of the potential hill, the portion that is typically used for deceleration (low phase), is always convex meaning that as the molecules climb the potential hill and, consequently, decelerate they simultaneously experience defocusing along the x-axis.

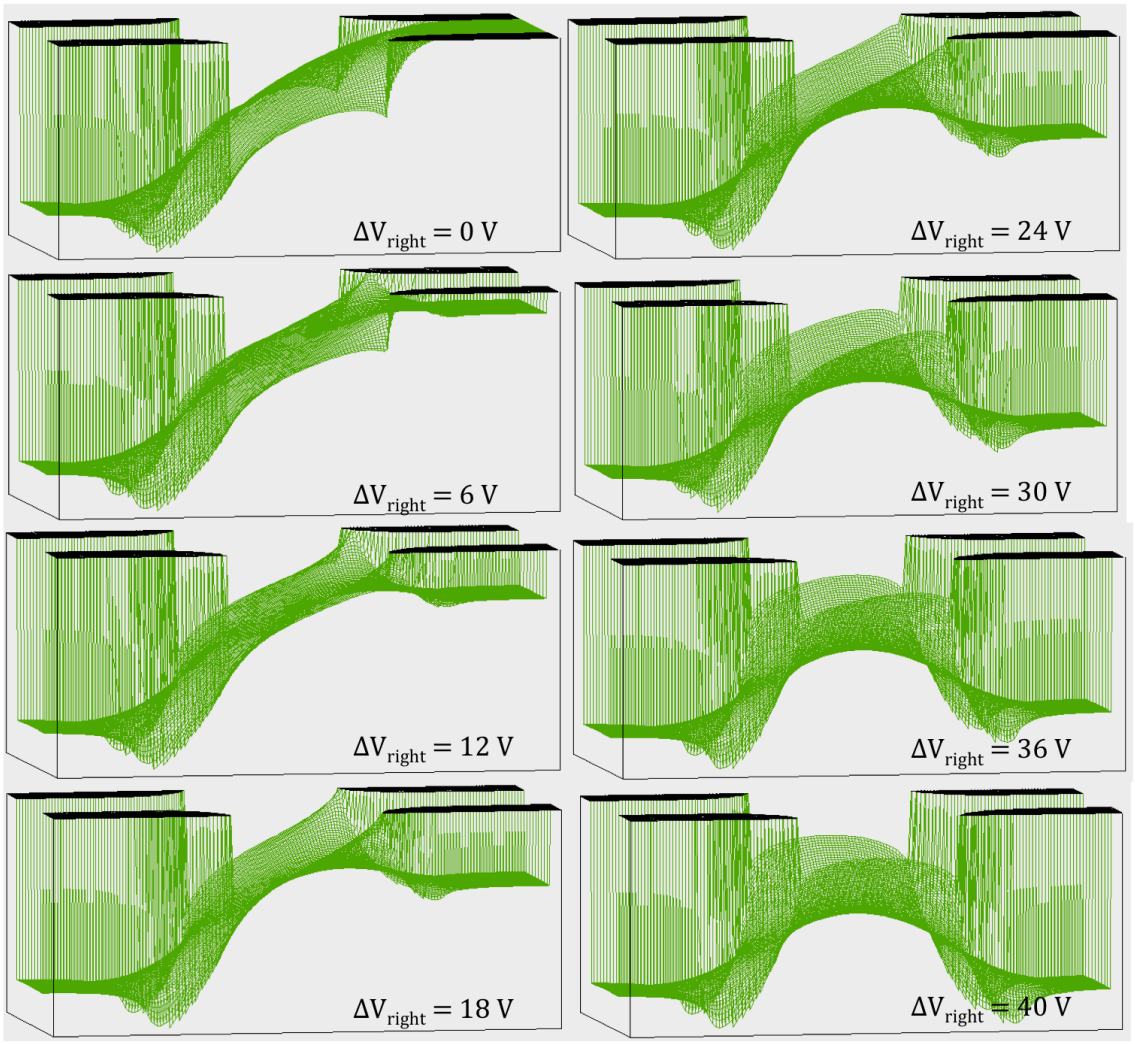

Figure 19. Potential Energy Surface Seen by HCN-like Molecule in a HFS Quantum State as a Function of Applied Voltage. The electrodes on the left maintain a potential difference of 40 V while the potential difference between the electrodes on the right is gradually increased from 0 V to 40 V. The molecules would fly through the lens either from left to right or from right to left.

In typical deceleration schemes the molecule never reaches the top of the hill. Since we can create focusing regions along the potential energy hill (typically in the gap between electrode pairs, see Figure 20a), the idea was to let the molecules fly over the

top of the hill and stop them on the other side, so that they get focused transversely. However, stopping the molecules on the down slope of the hill would defocus them longitudinally. The longitudinal and transverse stability may be maintained however, if we alternate our deceleration scheme (see Figure 20b), so that in all odd stages we stop the molecule on the up-slope of the hill (longitudinal focusing, transverse defocusing) and in all the even stages we stop the molecule on the down-slope of the hill (longitudinal defocusing, transverse focusing). This deceleration scheme then becomes similar to APF.

We performed a 1D trajectory simulation on CoMP2 program to see if the longitudinal stability could be achieved using this new scheme. Figure 21 shows the results. At the time we were unable to perform proper 3D simulation to see if transverse stability is also achieved. The molecules (HCN-like in HFS state) are entering a 100-stage device along the beam axis and with an initial uniform velocity distribution of 200 $\pm$5 m/s. Stage-100 is the first stage a molecule encounters with Stage-1 being the last. We clearly see that a longitudinal phase-space bucket is created and maintained even at stage-5. Therefore, it is possible to achieve longitudinal stability using this APF-like scheme but further simulations need to be done to study transverse stability. It may be true that the particle capture interval, where the particle is decelerated/accelerated and transversely focused at the same time, turns out to be very small. This is similar to the charged particle APF scheme where the accelerated particles tend to fall into ineffective phases of the accelerating field, where considerable defocusing occurs.

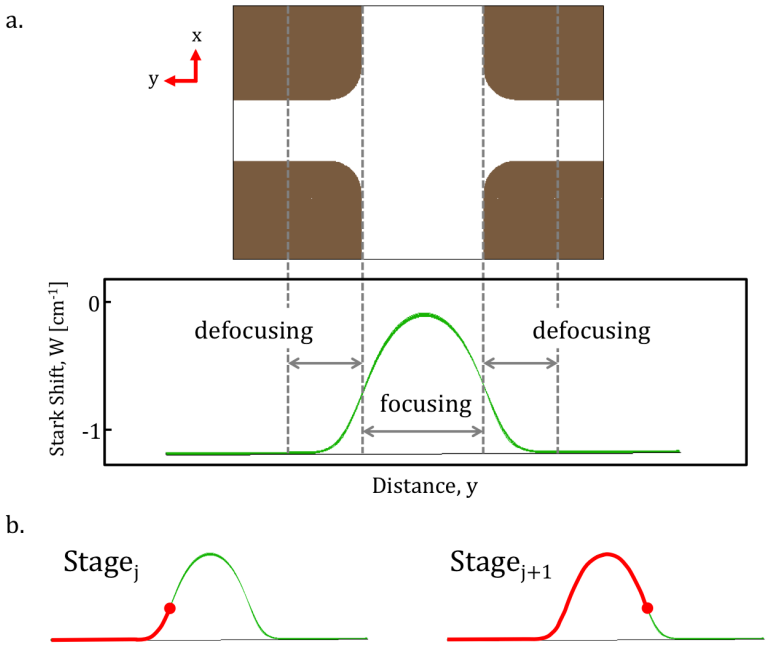

Figure 20. Proposed APF Deceleration Scheme. (a) A diagram showing the lens and a corresponding potential energy curve. Transverse focusing and defocusing regions are indicated. (b) Proposed deceleration scheme where we alternate between stopping the molecules on opposite sides of the hill.

The problem was essentially solved by incorporating asymmetry into longitudinal structure of the accelerating-focusing period for example, by introducing a constant into the synchronous phase value [76], by periodically changing the amplitude of the accelerating field [77], or by introducing a special function in the synchronous phase change [78].

3.5 Conclusions

It is possible to manipulate polar molecules using electric fields. We have outlined how one may control molecule's transverse motion using alternating gradient (AG) method and discussed how to construct suitable electrode geometry for efficient AG

focusing. In order to achieve focusing using the AG method, the gradient of the electric field has to be periodically rotated 90 degrees. This can be achieved in two different ways. We looked at the z-shaped geometry where the rotation of the field is accomplished by rotating the corresponding electrode segments in a two-electrode configuration. Analysis showed that this electrode structure could produce strong longitudinal gradients for efficient deceleration and moderate transverse gradients for focusing. We've also looked at the RFQ-type electrode geometry in a four-electrode configuration. This geometry is likely to result in the best transverse focusing but only moderate deceleration/acceleration as compared to the z-shaped geometry. Another advantage of the RFQ-type geometry over the z-shaped geometry is that the former can control transverse focusing essentially independent of the molecule's forward motion. On the other hand, the z-shaped geometry is easier to construct and only requires two electrode pads, one on the top and one on the bottom plate (versus 4, for the RFQ-type). A brief theoretical analysis of the transverse motion was also presented.

It should be noted that the theoretical methods presented for designing the electrode geometry are only useful as a starting point. With the advent of numerical methods the analytical expressions for the fields and potentials are no longer necessary. For most of the nontrivial geometries such analytical expressions are either not available or not possible to obtain. Optimization of the electrode geometries and their positioning within the device should be carried out using numerical optimization algorithms that iterate over variations in electrode geometry, electrode spacing and applied voltage. This would lead to a numerical simulation and optimization of the entire transport line as is done in designing modern particle accelerators.

Finally, we've looked at another method for achieving longitudinal and transverse stability using only accelerating fields. This method is similar to the alternating phase focusing (APF) used in charged particle accelerators, but applied to the case of polar molecules. We've demonstrated that it is possible to achieve phase stable deceleration using an APF-like approach but were not able to confirm transverse focusing. This method may prove to be useful in microchip decelerators-accelerators as it requires no additional focusing elements or complicated electrode arrangement.

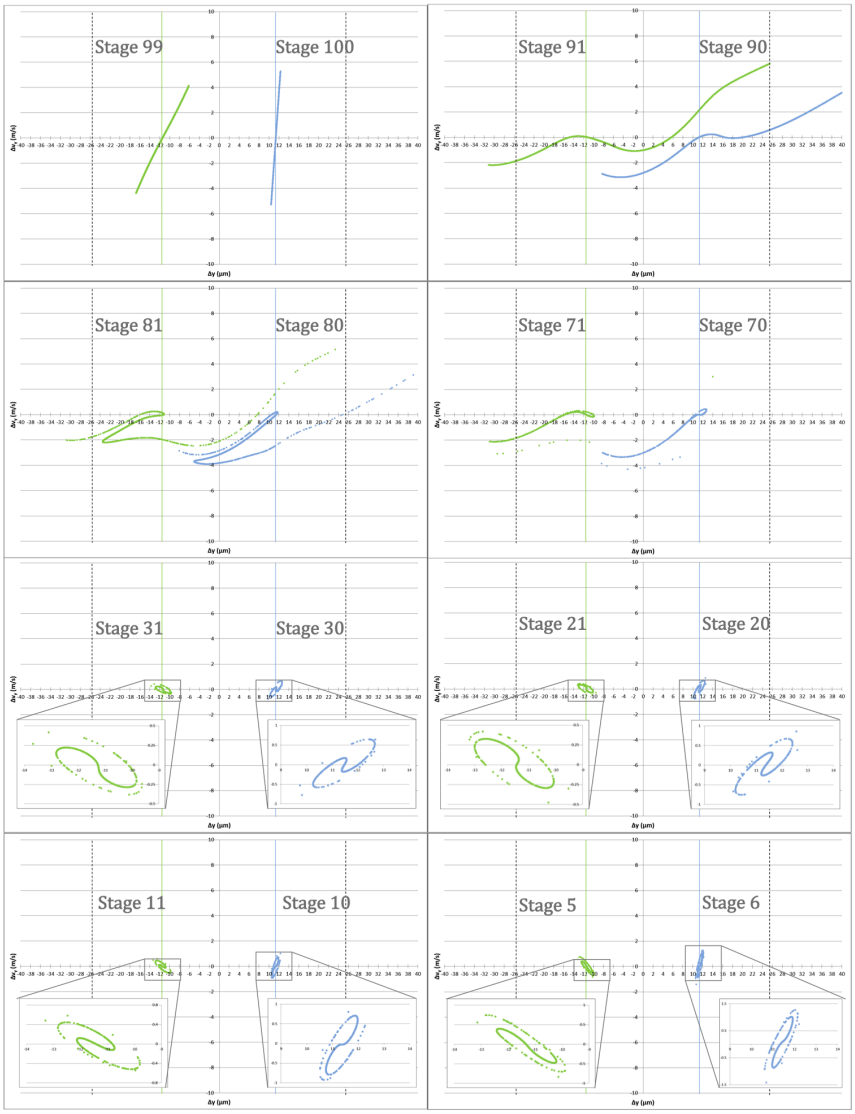

Figure 21. Longitudinal Phase-Space Diagrams for APF-like Scheme. The scheme alternates between decelerating on the up-slope in the odd stages (green data points) and down-slope in the even stages (blue data points). The vertical green and blue lines indicate the location of the synchronous particle inside odd or even stages, respectively. We superimpose data from even and odd stages on one phase-space diagram for ease of comparison. The positions are indicated relative to the center of the potential hill (middle of the gap between electrode pairs). The inserts, on some of the diagrams, show a magnified view of the phase-bucket. Dashed vertical lines indicate the extent of the potential energy hill.

CHAPTER IV

BEAM PROPERTIES, EXPERIMENTAL SETUP AND NUMERICAL SIMULATION

4.1 Properties of the Incoming Molecular Beam

There exist a number of methods for producing cold beams of various species of atoms and molecules. In principle, an atomic or molecular beam is nothing but a "leak in a vacuum system" [79]. It is formed by passing gas from a high-pressure container into an evacuated chamber through a small aperture. Using either the Reynolds number or the mean free path (λ) and aperture diameter (d) it is possible to categorize various types of the resultant flow into roughly three regimes: fully hydrodynamic regime ($50\lambda \leq d$), partially hydrodynamic regime ($1\lambda \leq d \leq 50\lambda$) and an effusive regime ($\lambda \geq d$) resulting in supersonic, buffer gas and effusive beams, respectively [80].

For the purposes of this thesis we can differentiate the three types based on the resultant forward velocity, see Figure 22. Supersonic beam expansion results in a very narrow forward velocity spread and therefore produces some of the coldest beams (~ 100 mK), which, due to enthalpy conservation, travel at supersonic velocities. The forward velocity can be reduced significantly, however, with seeding and by lowering the temperature of the source.

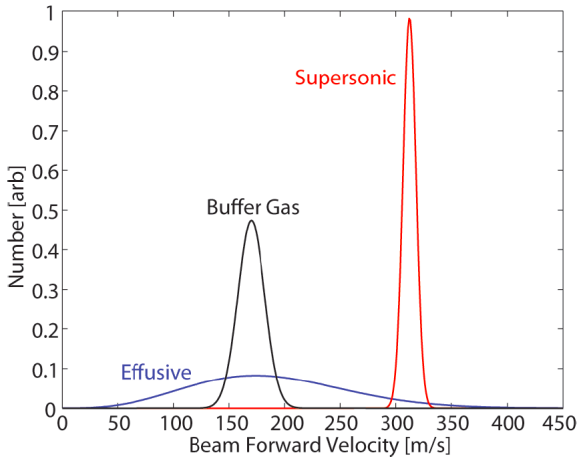

Figure 22. Schematic Velocity Distribution for the Three Types of Beams. The effusive beam is a simulated room temperature source of a species with mass of 100 amu, and supersonic source uses room temperature xenon as the carrier gas. The buffer gas cooled beam properties are taken from a ThO source with neon buffer gas. Reproduced from [80].

For example, one of the standard supersonic sources is argon expanding from a 300 K cell or, in a more technically challenging scenario, xenon expanding from a 210 K cell achieving forward velocities of about 600 m/s and 300 m/s, respectively. In contrast, buffer gas beams have a somewhat larger forward velocity spread but a lower average forward velocity often in the 100 – 200 m/s range.

The effusive regime is characterized by the near absence of collisions in the escaping gas near the aperture. In this limit, the mean free path of the gas at steady-state conditions is much larger than the characteristic length scale (thickness of the aperture and aperture diameter). Therefore, the beam will retain the same velocity distribution and the same distribution over the rotational and vibrational degrees of freedom as that in the container (cell). Effusive beams have typical forward velocities of several hundred meters per second with a very large velocity spread, which often limits their immediate use. In addition, creating a purely effusive beam without using advanced

cell geometry can be challenging. In what follows, we will limit our discussion to supersonic and buffer gas beams only.

Molecules in their ground-states (electronic, vibrational or rotational) have very long lifetimes and therefore are some of the best candidates for effective trapping. Unfortunately, the proportion of molecules in those states in a room-temperature gas is minuscule. Since the microchip designs presented in this thesis have no mechanism for selectively populating the ground-states, one has to invoke a procedure that would, ideally, produce ground-state molecular samples prior to their entrance of the microchip. Both supersonic beams and buffer gas beams can efficiently accomplish this task. In order to simulate, as closely as possible, the realistic conditions encountered in the laboratory one must be able to properly characterize the molecular beam entering the microchip. Hence, I will summarize the relevant points of the supersonic beam expansion and the buffer gas methods and estimate the expected molecular beam parameters.

4.1.1 The Supersonic Beam

There already exists a substantial amount of literature on the topic of supersonic molecular beams. The summary that follows is based on the article by David Miller [81].

Typically, a sample-container holds a carrier gas and a seed gas, pertinent to the experiment, under high pressure of several atmospheres. The mixture is allowed to expand (continuously or pulsed) through a sub-millimeter opening (nozzle) in the container wall such that the entire process is approximately adiabatic and isentropic. This results in quenching (or cooling) of the translational, vibrational and the rotational degrees of freedom. In particular, the exiting beam has a high longitudinal (forward

direction) speed of about 1000 m/s with a narrow velocity spread and a highly populated rotational ground-state. It is worth noting that quenching of the vibrational degrees of freedom is inefficient compared to the translational and rotational degrees of freedom due to the large vibrational inter-level separations and, consequently, low probability of quantum transition during a single collision. Nonetheless, a substantial amount of molecules produced this way are in their absolute ground-state.

As a quantitative example, adiabatic cooling in an expansion can produce initial molecular beams with densities on the order of 10^{12} molecules/cm^3 [82] or, equivalently, 1 molecule/μm^3, in a single quantum state. Typically, the expanding molecular beam has to travel through the nozzle and a skimmer (or two) before arriving at the microchip. If one uses 40 μm nozzle and a single 400 μm skimmer ($\theta = 1^\circ$) with 6.5 atm of stagnation pressure then a longitudinal translational temperature of $T_{long} = 1K$ and a perpendicular translational temperature of $T_{perp} = 0.1K$ may be expected; corresponding to the velocity spread of about 10% and 1%, accordingly.

Generally speaking, effective implementation of the seeded supersonic expansion method requires reduction in the temperature of the sample gas and a use of an appropriate heavy noble gas (argon, krypton or xenon) as a carrier. Under these conditions translational and rotational temperatures of a few tenths of Kelvin are readily achievable in practice. There are also a few limitations to the method. Perhaps the main limitation for achieving lower temperatures of the beam is the formation of the clusters among the seed gas molecules and between the seed gas and the carrier gas molecules. These weakly bound van der Waals complexes are the result of a three-body collision with a third body carrying off the energy.

Maximization of the cluster formation is achieved when the gas becomes supersaturated leading to condensation. Although the phenomenon of condensation is complex, for our purposes cluster formation is facilitated when one increases the container pressure, decreases the nozzle diameter or lowers the temperature in a non-isentropic way [83].

Figure 23 shows the complicated features of a free jet expansion under continuum conditions. The existence of various shock structures complicates the experimental implementation. Nonetheless, if the skimmers are to be placed within the so-called zone of silence, where the expansion flow is approximately isentropic with negligible viscous and heat conduction effects, then the difficulties arising from the shock structures may be significantly reduced. Particles in the sample container start in the stagnation state (P_0, T_0) with very small velocity but are accelerated toward the exit by the imposed pressure difference $(P_0 - P_b)$, where P_b is the background pressure. In general the flow speed at the exit may be subsonic, sonic or supersonic depending on how the pressure ratio P_0/P_b compares to a critical value $G \equiv \left(\frac{\gamma+1}{2}\right)^{\frac{\gamma}{\gamma-1}}$, where γ is the heat capacity ratio C_p/C_v. The critical value is less than 2.1 for all gases, hence the accelerated flow is supersonic if $P_0/P_b > 2.1$ and the exit pressure becomes independent of P_b tending towards $P_0/G \approx 0.5P_0$.

Using thermodynamic analysis one can arrive at the expressions characterizing the molecular beam from the supersonic expansion. Several assumptions go into the analysis such as that the flow is adiabatic and isentropic, ideal gas behavior, continuum flow and temperature independence of C_p. High density and collision frequency of the flow allow one to define density, equilibrium temperature etc., and thereby satisfy the continuum assumption.

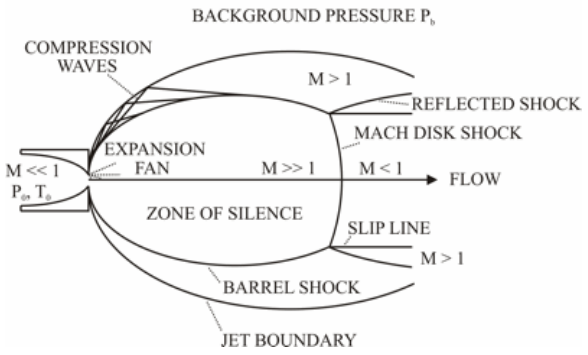

Figure 23. Shock Structures in a Supersonic Expansion. Reproduced from [81].

Since gas expands without exchanging heat with its surroundings and the effect of gas viscosity is negligible (adiabatic, isentropic assumption), it follows that the sum of the enthalpy, H, and the kinetic energy of the mass flow must be conserved (first law of thermodynamics):

$$H(z) + \frac{1}{2}mv(z)^2 = const \tag{4.1}$$

where $H(z)$ is the enthalpy of the gas at position z from the nozzle along the beam's center line and $v(z)$ is the average flow speed at position z. We wish to obtain an expression for the average flow speed under all the assumptions stated above.

Since the enthalpy per particle may be a function of temperature and pressure, the differential can be written as

$$dH(T,P) = \left(\frac{\partial H}{\partial T}\right)_P dT + \left(\frac{\partial H}{\partial P}\right)_T dP = C_P(T,P)dT + \left(\frac{\partial H}{\partial P}\right)_T dP \tag{4.2}$$

where $C_P = \left(\frac{\partial H}{\partial T}\right)_P$ is the heat capacity per particle at constant pressure. On the other hand, from the definition of enthalpy it follows that

$$\left(\frac{\partial H}{\partial P}\right)_T = T\left(\frac{\partial S}{\partial P}\right)_T + V. \tag{4.3}$$

We are assuming that the gases involved in the process can be approximated as ideal, obeying the equation of state for ideal gases $P = kT/V$, where P is pressure, V is volume per particle, T is temperature and k is the Boltzmann constant. Using Gibbs free energy, G, we see that for an ideal gas

$$\frac{\partial^2 G}{\partial P \partial T} = -\left(\frac{\partial S}{\partial P}\right)_T = \left(\frac{\partial V}{\partial T}\right)_P = -\frac{k}{P} = -\frac{V}{T}. \tag{4.4}$$

Consequently,

$$\left(\frac{\partial H}{\partial P}\right)_T = 0. \tag{4.5}$$

With this conclusion we see that our expression for, dH, simplifies to $dH = C_P(T)dT$ i.e. enthalpy per particle depends only on the temperature. It now follows that if, during the expansion of our ideal gas, all the enthalpy was converted into kinetic energy then the maximum possible speed, v_{max}, may be determined from,

$$\frac{1}{2}mv_{max}^2 = H(z=0) = \int_0^{T_0} C_P(T)dT. \tag{4.6}$$

Table 1. Comparison of Candidate Molecules and Their Maximum Speeds in Supersonic Expansion. Data obtained from Dartmund Data Bank by DDBST GmbH.

	HCN	C_2H_3N
Mass [amu], m	27.026	41.053
Heat capacity at 1 atm [J/mol·K], C_P	71.0	76.6
Temperature [K], T_0	300	303
Maximum speed [m/s], v_{max}	1256	1062

This expression may be simplified even further by noting that, aside from the two extremes of very high and very low temperatures, C_P can be assumed to be independent of temperature and hence,

$$v_{max} = \sqrt{\frac{2C_P T_0}{m}}. \tag{4.7}$$

Here, T_0 is the initial temperature of the gas. For our current molecular candidates, hydrogen cyanide (HCN) and acetonitrile (C_2H_3N), parameters and possible maximum speeds obtained from supersonic expansion are summarized in Table 1.

From an experimental point of view it is desirable to reduce the velocities even further prior to loading the microchip. According to equation (4.7), the reduction is possible if one lowers the temperature of the gas in the sample container (source) or lowers the heat capacity or increases the mass. Lowering the temperature of the gas in the source is relatively easy. If the source temperature of 100 K were used instead of the room temperature then the corresponding maximum speeds of HCN and C_2H_3N would be 725 m/s and 612 m/s, respectively.

Table 2. Maximum Speeds of the Candidate Molecules from a Seeded Supersonic Expansions in 80% and 95% Mixtures of Xe or Kr Carrier Gas.

	HCN, [m/s]	C_2H_3N, [m/s]
80% Krypton, (T = 360 K)	473	467
95% Krypton, (T = 360 K)	447	447
80% Xenon, (T = 360 K)	450	434
95% Xenon, (T = 360 K)	360	360

It's impossible to change the mass or the heat capacity of the relevant molecule, however, if one uses a mixture of two gases then the above equations are still valid but quantities such as mass and the heat capacity must be replaced by the two-gas averages. This technique is known as seeding. In particular, if one uses a small fraction of the seed gas (HCN or C_2H_3N) in a noble carrier gas (Ar, Kr, Xe) and the mixture is expanded then, the maximum velocity will be determined predominantly by the properties of the carrier gas.

Typically, to achieve the lowest possible speed one conducts the expansion at a temperature slightly above the boiling point of the mixture. Since the boiling points of the three noble gases are relatively low Ar(102 K), Kr(140 K), Xe(165 K) compared to the boiling points of our sample gases HCN(300K) and C_2H_3N(356 K) this implies that our limiting factor is the seed molecule(s). If we used a 20% HCN (C_2H_3N) seeded in 80% xenon (m_{Xe} = 131.3 amu) at a temperature of 360 K then we would obtain maximum speed of 450 m/s (434 m/s). Table 2 summarizes the maximum speeds for seeded expansions in 80% and 95% mixtures of Xe or Kr (m_{Kr} = 83.798 amu) carrier gases.

Note that because C_2H_3N is relatively heavy we cannot use argon as the carrier gas since, in that case, the mixture would result in higher speed after the expansion as

compared to unseeded expansion. Overall, Ar would be of little assistance in lowering the speed when used with either HCN or C_2H_3N.

As a final note, knowing the Mach number, M, enables one to compute all thermodynamic variables. Mach number is the ratio of the flow speed, v, to the local speed of sound, a. For an ideal gas, $a = \sqrt{\frac{\gamma n R T}{m}}$, and since $M \equiv \frac{v}{a}$ then thermodynamic variables can be calculated from:

$$\frac{T}{T_0} = \left(\frac{P}{P_0}\right)^{\frac{\gamma-1}{\gamma}} = \left(\frac{\rho}{\rho_0}\right)^{\gamma-1} = \left[1 + \frac{\gamma-1}{2}M^2\right]^{-1} \tag{4.8}$$

where T_0, P_0, and ρ_0 are the temperature, pressure, and density of the source; T, P, and ρ are the same quantities in the zone of silence; γ is the heat capacity ratio.

4.1.2 The Buffer Gas Beam

A good treatment of buffer gas cooled beam production and properties is provided in Reference [80]. Here, we briefly summaries all of the salient points presented in that article.

Typically, buffer gas beams operate in a partially hydrodynamic regime where enough collisions occur to modify the beam properties from those present in the cell without causing the flow to become fluid-like. It is possible, however, to produce buffer gas beams in all three regimes. Compared to the supersonic beam expansion, buffer gas beam production fundamentally differs in its approach to cooling molecules.

A cold cell, with typical dimensions of a few centimeters, contains an inert"buffer" gas atoms cooled to 2 – 20 K by the cold cell. Hot molecules of interest are introduced into the cold cell at a typical initial temperature between 300 and 10,000 K through a

number of methods, including laser ablation, light-induced atomic desorption, beam injection, capillary filling, and discharge etching. The number density of the buffer gas atoms, inside the cold cell, is maintained at $10^{14} - 10^{17}$ cm^{-3}. This number density is low enough to prevent cluster formation caused by the three body collisions, which is one of the major limitations in supersonic beam expansion, and yet high enough so that thermalization occurs prior to molecules hitting the walls of the cold cell. In contrast, a number density of the molecules is $< 1\%$ of the number density of the buffer gas. Similar to the case of the seeded supersonic expansion, such low number density of the molecules of interest allows one to treat them as a trace component, with the gas flow properties being determined solely by the buffer gas. If the molecules and the buffer gas are allowed to escape the cell, through a few millimeter-sized opening (orifice), faster than the diffusion time then a cold molecular beam can be formed. In the case of the beam with pulsed loading, the duration of the molecular pulse is determined by the extraction time, which is generally around 1 – 10 ms.

It is useful to use the Reynolds number to characterize gas flow. The Reynolds number is defined as the ratio of inertial to viscous forces in a fluid flow:

$$Re = \frac{T_{inertial}}{T_{viscous}} = \frac{\rho w^2 d^2}{\mu w d} = \frac{\rho w d}{\mu} \tag{4.9}$$

where ρ is the density, w is the flow velocity, μ is the (dynamic) viscosity, and d is the aperture diameter. Near the aperture, the Reynolds number can be related to the mean free path λ and aperture diameter d as, $Re \approx 2d/\lambda$.

The forward velocity of the molecules in the buffer gas beam is usually smaller than those in the supersonic or effusive beams, depending on the Reynolds number of the buffer gas flow. The behavior is schematically shown in Figure 24.

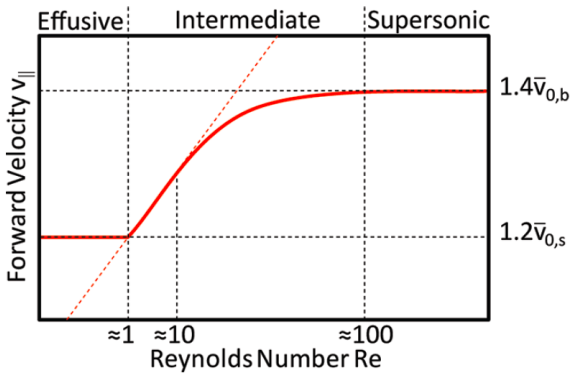

Figure 24. Schematic Representation of Beam Forward Velocity as a Function of Reynolds Number. Reproduced from Reference [80].

In the intermediate regime, the collisions between the molecules and the buffer gas atoms, near the aperture, are primarily in the forward direction. As a result, molecules can be accelerated to a forward velocity, $v_{||,s}$, which is larger than the thermal velocity of the molecules $\bar{v}_{0,s} = \sqrt{\frac{8k_BT}{m_s\pi}}$.

For $1 \leq Re \leq 10$, there are few collisions between the molecules and the buffer gas atoms, whose average velocity is $\bar{v}_{0,b}$. The forward velocity of the molecules, to the first order of approximation, have a linear dependence on Re,

$$v_{||,s} \approx 1.2\bar{v}_{0,s} + 0.6\bar{v}_{0,b}Re\frac{m_b}{m_s} \tag{4.10}$$

where m_b is the mass of the buffer gas atom and m_s is the mass of the molecule of interest. The linear model breaks down, however, as $v_{||,s}$ approaches $\sim \bar{v}_{0,b}$ and the number of collisions increases. In this case, one can use "sudden freeze" model [84], where it is assumed that the molecules are in equilibrium with the buffer gas until the point along the beam where there are no more collisions and the beam properties stop changing or "freeze".

Then, the dependence of the forward velocity of the molecules on the Reynolds number can be given by

$$v_{||,s} \approx 1.4\bar{v}_{0,b}\sqrt{1 - 4Re^{-4/5}} \tag{4.11}$$

For HCN molecules in a helium buffer gas at 5 K with $Re = 50$, the calculated forward velocity is around 200 m/s. In the limit of very large Reynolds number ($Re \geq 100$) one approaches the supersonic flow regime, where there are enough collisions to accelerate the molecules to the full forward velocity of the buffer gas, $v_{||,s} \approx v_{||,b} \approx 1.4\bar{v}_{||,b}$.

4.2 Numerical Electrostatic Potential and Electric Field Calculations

The electrostatic potential, three-dimensional electric field and field gradients are all calculated using charged particle optics simulation software SIMION® version 8.1. This segment of the program works by solving Laplace equation with the electrodes constituting the boundary conditions and using over-relaxation finite difference and skipped-point refining techniques.

SIMION utilizes square or cubic grids with equally-spaced points constituting an array. Each point within an array caries two types of information: voltage and point-type. The latter allows the program to distinguish between an electrode and a non-electrode point. A user starts out by defining the size of the array, the geometry of the electrodes and the voltage at each electrode. Then the program implements the finite difference technique that uses the average potential of the nearest four (2D arrays) or six (3D arrays) neighboring points to estimate the potential of each non-electrode point within the potential array (PA). Each scan through an array constitutes an iteration.

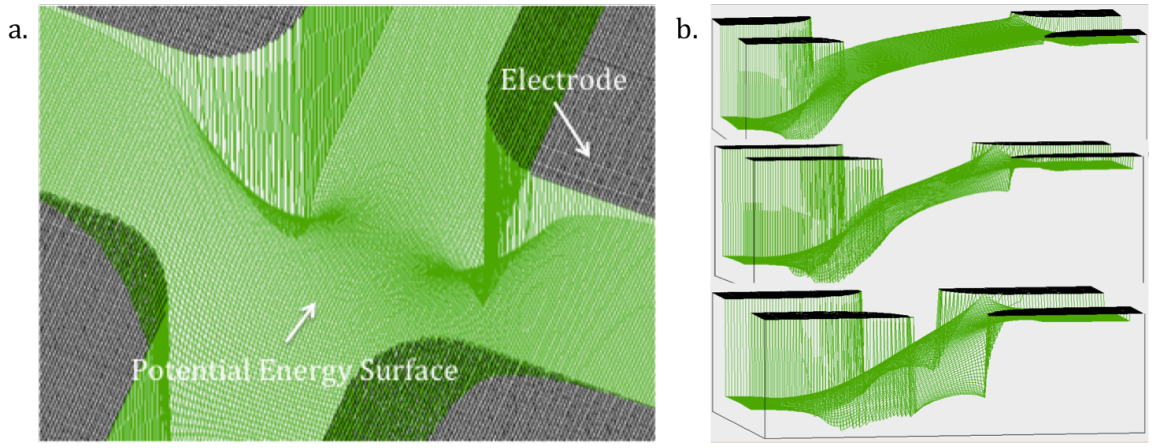

Figure 25. Example Electrode Geometry and the Resultant Potential Energy Surface Visualized Using Rubber-Sheet Style of Display. See text for details.

With each successive iteration of the procedure, the potentials of the electrode points are propagated further throughout the potential array until pseudo-equilibrium is reached when potential values no longer change appreciably in a single scan. At this point the convergence tolerance has been reached and all non-electrode points contain appropriate potentials corresponding to a solution of the Laplace equation. The solution may be visualized using rubber-sheet style of display which aids in developing an intuitive model for particle behavior, see Figure 25a.

This mode of visualization is especially helpful in identifying promising electric field or Stark potential configurations by experimenting with different electrode geometries and parameters. For example, one can easily see what effect changing separation distance between the electrode stages has on the magnitude of the transverse (confining) and longitudinal forces which are related to the curvature of the potential energy surface, see Figure 25b. In particular, we see that as the particles approach the inter-stage gap (say, from left to right) they encounter an initially convex (de-

focusing) hill, which, nonetheless, can become focusing at the top if the stages are brought closer together. Ultimately, it is desirable to simulate the entire beamline and to optimize the position, geometry and stage spacing to yield, for example, the maximum throughput.

It should be noted that prior versions of SIMION contained significant loss in field accuracy near the electrodes if the electrode surface didn't perfectly align with the potential array grid cells. The only way around this issue was to increase the grid density (for the entire PA), which came at a significant, often prohibitive, memory cost. These inaccuracies noticeably distorted fields, in the near field region, resulting in unrealistic trajectories. Small scale of electrodes and small inter-electrode separation distances, used in our experiments, made our simulations particularly sensitive to this issue. The latest version of SIMION (8.1), however, uses a new "surface enhancement" feature with fractional grid units. This feature improves accuracy by at least an order of magnitude making it compatible with our experimental requirements. It is also true that the procedure for solving the Laplace equation is fundamentally an averaging process and, as a result, tends to smooth out values in the far-field region due to surface irregularities. We present specific results on the electric fields and gradients in Chapter III. For molecules with initial position close to the electrodes and for those that venture far from the beam axis, a careful attention must be paid to exclude inauthentic trajectories. When possible it is a good practice to exclude all trajectories that approach the electrode surfaces within 2 grid units.

It is also possible to improve the accuracy of the simulation even further by using multiple nested PA instances with different grid densities. For example, higher grid density PAs can be used in the areas where the potential energy gradients are large

corresponding to a rapidly changing (spatially) electric field. This is typically the case around sharp corners or small oscillating surface features. Following this nested-PA approach would provide the best accuracy while keeping the simulation time reasonable and is, in general, preferable over increasing the overall grid density within a single PA. The drawback is in an added complexity, since the nested PAs have to be properly stitched together, and in that the information about the "trouble" spots (such as corners) has to be known ahead of time. In the following section, we discuss how trajectories are determined using the numerically calculated electric fields and field gradients.

4.3 Calculation of Forces and Trajectories in an Inhomogeneous Field

SIMION, by design, is a native environment for carrying out charged particle (ion) simulations and therefore cannot be immediately used for simulating dynamics of neutral particles. In order to simulate beams of neutral (polar) molecules in inhomogeneous electric or magnetic fields without compromising the sophisticated built-in routines one must 'trick' SIMION into thinking that it is dealing with charged particles. There are two ways by which the trick can be accomplished: *potential array (PA) modification* and *acceleration modification*. Our group has pursued both methods at various stages of project development.

Modifying acceleration requires writing a program that runs inside SIMION Ion Optics Workbench (IOB), that during particle flying, replaces the acceleration vector seen by the particles with a new acceleration vector obtained from a user defined equation. In particular, given the input geometry of the electrodes, SIMION will solve Laplace's equation obtaining the electric potential V at every point in a potential array. The force on the charged particle will then be proportional to the gradient of

the electric potential. For neutral (polar) particles the force is instead proportional to the gradient of the electric field $|\vec{E}|$ or, more precisely, to a scalar function of the electric field called Stark potential $U(E)$. From this function one can determine the explicit form of the force on the neutral particle and, hence, determine the expressions for acceleration:

$$\vec{F} = -\vec{\nabla} U(|\vec{E}|) \tag{4.12}$$

$$\vec{F} = -\frac{dU}{dE}\vec{\nabla} E = -\left(\frac{1}{E}\frac{dU}{dE}\right)\left(\frac{1}{2}\vec{\nabla} E^2\right) \tag{4.13}$$

We wish to express the above equation in terms of the electric potential that SIMION recognizes. Since, $\vec{E} = -\vec{\nabla} V$ and $\vec{F} = m\vec{a}$, one can explicitly evaluate the gradient of the electric field squared in terms of V and rewrite the result in a compact matrix form:

$$\begin{pmatrix} a_x \\ a_y \\ a_z \end{pmatrix} = -\frac{1}{m}\left(\frac{1}{E}\frac{dU}{dE}\right)\begin{pmatrix} \frac{\partial^2 V}{\partial x^2} & \frac{\partial^2 V}{\partial x \partial y} & \frac{\partial^2 V}{\partial x \partial z} \\ \frac{\partial^2 V}{\partial y \partial x} & \frac{\partial^2 V}{\partial y^2} & \frac{\partial^2 V}{\partial y \partial z} \\ \frac{\partial^2 V}{\partial z \partial x} & \frac{\partial^2 V}{\partial z \partial y} & \frac{\partial^2 V}{\partial z^2} \end{pmatrix}\begin{pmatrix} \frac{\partial V}{\partial x} \\ \frac{\partial V}{\partial y} \\ \frac{\partial V}{\partial z} \end{pmatrix} \tag{4.14}$$

where m is the mass of the molecule. At this point, one would need to know the functional form of the Stark shifts for the molecular levels of the molecule of interest obtained from quantum mechanical calculations or its approximate form.

For example, assuming that our system (molecule in a particular rotational or translational state) can be well approximated as a two-state system with some dipole moment μ. We can write down a general form for the potential energy function:

$$U(E) = U_0 \pm \sqrt{A^2 + (\mu_{eff}E)^2} \tag{4.15}$$

where U_0 is the energy of the unperturbed, particular degenerate state of the system, A is the energy associate with lambda-doublet, inversion frequency, etc., and μ_{eff} is the effective dipole moment of the molecule subject to the field. With this we arrive at the final formulation for the acceleration:

$$\begin{pmatrix} a_x \\ a_y \\ a_z \end{pmatrix} = \pm\frac{1}{m}\left(\frac{\mu_{eff}^2}{\sqrt{A^2 + (\mu_{eff}E)^2}}\right) \begin{pmatrix} \frac{\partial^2 V}{\partial x^2} & \frac{\partial^2 V}{\partial x \partial y} & \frac{\partial^2 V}{\partial x \partial z} \\ \frac{\partial^2 V}{\partial y \partial x} & \frac{\partial^2 V}{\partial y^2} & \frac{\partial^2 V}{\partial y \partial z} \\ \frac{\partial^2 V}{\partial z \partial x} & \frac{\partial^2 V}{\partial z \partial y} & \frac{\partial^2 V}{\partial z^2} \end{pmatrix} \begin{pmatrix} \frac{\partial V}{\partial x} \\ \frac{\partial V}{\partial y} \\ \frac{\partial V}{\partial z} \end{pmatrix} \tag{4.16}$$

We must now solve the first and second order partial derivatives with some numerical approximation scheme. SIMION uses a standard fourth order Runge-Kutta method, with variable time step, to solve partial and ordinary differential equations for numerical integration of the particle's trajectory in three dimensions. A similar scheme could be implemented within the acceleration modification program running inside the workbench. Otherwise the integration errors associated with the chosen numerical scheme will be higher than those in PA modification method (which uses 4^{th} order Runge-Kutta method). Finally, the actual replacement of the acceleration vector with the newly calculated one is done within SIMION's *accel_adjust* segment.

Then at each time step the program looks up the appropriate acceleration value for that point along the trajectory and uses it to get to the next point after which the whole process repeats until the molecule reaches the end of the potential array or crashes into one of the electrodes.

An alternative method is to modify an entire potential array as a separate batch mode program that runs once prior to loading the PA in a workbench and have SIMION calculate the particle trajectories in the usual way. This method is easier to implement and guarantees proper integration with the rest of the SIMION core routines. After SIMION obtains solution to the Laplace equation for the electric potential from the electrode geometry of choice, the batch mode program replaces all of the electric potential values stored in a PA with the values derived from the potential energy function $U(E)$, as expressed in Equation 4.15. Then this new, modified PA is loaded into the IOB for subsequent trajectory simulation using fourth-order Runge-Kutta method with binary boundary approach algorithm and field curvature detection for minimizing the number of integration steps and minimizing errors around sharp edges (or other higher field curvature areas).

4.4 Lua Simulation Programs

An accurate description of the motion of particles inside the microchip requires having accurate three-dimensional electric field calculations (Section 4.2), Stark shifts of the molecular levels or an approximate functional form and three-dimensional trajectory calculations (Section 4.3). All this information is assembled within the simulation program, which also must provide proper time dependence to the electric fields. We've created two different programs *CoMP1* and *CoMP2*, to carry out the simulations within SIMION, using Lua programming language.

Simulation studies presented in Chapter II were obtained using CoMP1. The program is composed of two parts, a batch-mode segment and a workbench segment. In the batch-mode segment the entire device, with 100 or so stages, is created inside a single PA using *pa:fill{}* function with fractional surface feature. This function can, in principle, create electrodes with complex geometry, but in practice it is better to use geometry files (GEM), that is an ASCII file that uses a 3D solid geometry modeling language, to define the desired electrode array geometry. Doing this avoids introduction of jags when the electrodes are scaled or when various symmetries are applied in combination with fractional surface features.

In general, as the particle flies through the microchip it may encounter two (or more) different electric field configurations that depend on the applied voltage polarity. The time dependence, of the overall electric field, is introduced when the field is cycled between the first configuration and the second configuration. Therefore, an important function of the simulation program is to provide proper time-dependence of the electric field. In CoMP1 this is accomplished by creating a second PA containing the exact copy of the device. Then the remaining portion of the batch-mode segment replaces the electric potential from the first configuration with the appropriate Stark potential (see, Section 4.3) for the first PA while the potential values in the second PA are adjusted, in like manner, as dictated by the second configuration. For example, we may want to simulate a scenario where the electrodes are turned ON for some period of time and then turned OFF for some period of time. In that case, the first configuration would contain electric field values according to the magnitude and polarity of the applied voltage, whereas the second configuration would contain all zeros (since the voltage is turned off). Our batch-mode segment would then create two PAs, each

containing the device, and populate the first PA with the appropriate Stark potential values whereas the second PA would contain all zeros. The switching between the two configurations is accomplished in the workbench segment as explained below. When done, the batch-mode segment creates and loads in the IOB, side-by-side, two PAs containing Stark potentials that are ready for subsequent trajectory calculations.

The second portion of the CoMP1 program, the workbench segment, takes over upon completion of the batch-mode segment and when the particles begin to fly through the device. A user specifies the desired duration of the ON and OFF time periods that the workbench segment uses as the input parameters. The particles are allowed to fly one at a time according to the initial spatial and velocity distribution. The master time-of-flight clock starts when the particle is initialized inside the PA (also known as the 'time of birth'). As the particle traverses the device, the workbench segment compares the value of the master clock with the specified value of the ON and OFF time periods. If the value of the master clock is a multiple of the OFF period then the workbench segment pauses the master clock and relocates the particle into the second PA, retaining all of the speeds (v_x, v_y, v_z) and relative position. The clock is again started and the particle is allowed to fly now inside the second PA until the value of the master clock becomes a multiple of the ON period. When that happens, the master clock is paused and the particle is relocated into the first PA and the whole cycle repeats until the particle reaches the end of the device or crashes into an electrode, see Figure 26.

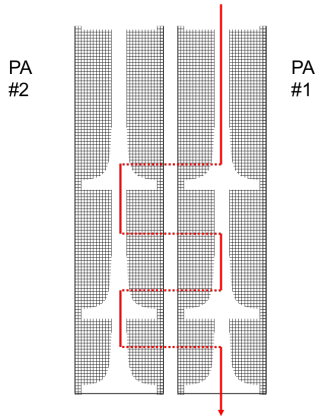

Figure 26. Diagram Illustrating how Time-Dependence of the Electric Field (Stark Potential) can be Modeled for the Case when the Field is Switched from Configuration 1 to Configuration 2. In this case, one can duplicate PA #1, thereby creating PA #2, adjust all of the electric field (Stark potential) values in the new PA according to configuration 2 and then the time switching between the two configurations is accomplished by spatially relocating the particle (dashed line) from one PA to another.

The spacing of the stages (inter-stage spacing), in a type-B device, is directly related to the ON and OFF durations. In CoMP1, these time periods are calculated assuming a quadratic spatial dependence of the Stark potential encountered by the synchronous molecule. However, this approximation may be less appropriate for different electrode geometry and using a simple instantaneous impulse approximation often yields results that are in very good agreement with the quadratic potential approximation (see, Chapter II).

It should be noted that the integration time-step needs to be adjusted to make sure that the program does not miss either ON time or OFF time. This could be accomplished with a simple time-step adjusting routine such as:

```
if    ion_time_of_flight < timeON
then  ion_time_step = min(ion_time_step, timeON -
      ion_time_of_flight)
end
```

Finally, should the particle trajectory be terminated by hitting an electrode then the workbench program records to a file the particle's parameters such as position, speed, time-of-flight, etc. These parameters are then used by a separate program for analysis.

There are several limitations to CoMP1. Perhaps the biggest practical limitation is that the program attempts to simulate an entire device. This results in very large PA files that are too cumbersome to handle on a typical PC but perhaps are less of a problem if ran on multiple PCs or through the cloud. Also, since the total number of available grid points is limited, creating an entire device inside the PA lowers the possible grid point density, which in turn lowers the accuracy of the simulations. Additionally, the program can only handle simple switching between field configurations making it hard to simulate gradual switching or gradual voltage reduction. Finally, it would be desirable, for a given molecule, to not use any type of a priori approximation but instead use the actual 'shape' of the potential energy surface obtained numerically from a particular electrode geometry. CoMP2 was created to address these limitations.

Similar to CoMP1, CoMP2 is composed of two segments: batch-mode segment and a workbench segment. The comparison between the two programs is shown in Figure 27. Since we are focusing on the electrode structures in a microchip that are identical (varying, perhaps, only in length) then instead of creating an entire device inside a PA as it was done in CoMP1, CoMP2 creates a simulation cell.

CoMP1	CoMP2
Batch-mode segment:	**Batch-mode segment:**
1. Creates the *entire device* using pa:fill{}, inside PA #1, with fractional surface feature.	1. Creates *simulation cell* using pa:fill{}, inside PA #1, with fractional surface feature.
2. Creates PA #2 by duplicating PA #1, thereby creating two copies of the device.	2. Creates other PAs, if necessary, containing the same or different simulation cells.
3. Replaces electrostatic potential values, in each PA, with appropriate Stark potential values.	3. Replaces electrostatic potential values, in each PA, with appropriate Stark potential values.
4. Imports PAs into IOB.	4. Imports PAs into IOB.
Workbench segment:	**Workbench segment:**
1. Initializes user input parameters and particle distributions.	1. Initializes user input parameters and particle distributions.
2. Adjusts trajectory integration time step.	2. Adjusts trajectory integration time step.
3. Teleports flying particles between PA #1 and PA #2 to simulate time-dependent field.	3. Defines proper boundary conditions and looping protocols for the simulation cell. Defines teleportation protocol in the case of multiple PAs (or complicated field configurations).
4. Records particle parameters upon termination.	4. Couples and decouples the particles from the electric field via *ion_charge* function to simulate time-dependent field.
	5. Performs *pre-run* using a synchronous particle to determine time for traversing a portion of the potential hill thereby determining proper time ON and stage spacing.
	6. Records particle parameters upon termination.

Figure 27. Comparison of the Basic Structure of the Two Simulation Programs.

This simulation cell contains only those electrode structures that produce regions of inhomogeneous electric field. The idea being that in the regions where the electric field is sufficiently homogenous (or altogether absent) there are no significant forces on the neutral, polar particle.

Without acceleration, the particle trajectory evolves according to $\bar{r}(t) = \bar{r}_0 + \bar{v}_0 \cdot t$, where the final position $\bar{r} = (x, y, z)$ follows from the position $\bar{r}_0 = (x_0, y_0, z_0)$ and velocity $\bar{v}_0 = (\dot{x}_0, \dot{y}_0, \dot{z}_0)$ at the beginning of the homogenous region. Therefore, a computationally more efficient program would only simulate particles flying through inhomogeneous regions while computing trajectories in the other regions according to a simple equation.

Figure 28 shows an example z-shape electrode structure inside a three-dimensional simulation cell, a $z - y$ plane slice along the middle of that cell and a corresponding Stark potential function along the beam axis running through the middle of the cell. The batch-mode segment of the program works in the same way as in CoMP1 except that it creates one (or more) PAs containing only the simulation cell instead of the entire device. It should be noted that the PA files from CoMP1 and CoMP2 could be made to be comparable in size. In that case, however, the accuracy of the solution to the Laplace equation (especially near the corners and other small features) will be much higher in CoMP2 then CoMP1 due to higher grid density (see Section 4.2).

After loading PAs into the IOB the program performs a pre-run using a single "ideal" particle, the so-called synchronous particle. The particle starts out at a point p1 with a predefined longitudinal speed, traveling along the beam axis $\overline{p1p4}$. The point p1 marks the boundary between homogenous and inhomogeneous regions as defined by the Stark potential energy surface. When the particle reaches point p2 the program records various parameters, such as the time it took to go from p1 to p2, and then relocates the particle back to p1. Because during the passage from p1 to p2 the particle has climbed the potential energy hill, its kinetic energy is reduced by ΔW (see Figure 28c). Therefore, when relocated back to p1 the particle's speed

is reduced by $\sqrt{2\Delta W/m}$, where m is the mass of the particle. If this is done multiple times then one can bring the particle's final speed to any desired value. The other two points p3 and p4 are used in the case of an acceleration that is not slowing down the particle but rather accelerating it. The program then works in analogous manner except that the synchronous particle starts out at p3 and goes down the potential energy hill until it reaches point p4. In both cases, when the synchronous particle reaches the final speed, the pre-run is terminated. The data from the pre-run is used to determine the ON and OFF times and the proper spacing of the electrode stages. All this information is then used during the main-run.

Particles are created inside the cell with a predefined spatial and velocity distributions. Each, newly created, particle is positioned along the dashed line (a plane in 3D) running thought point p1 between the top and bottom electrodes. The program calculates the distance and the time the particle would take, based on its starting position and speed, to fly through the first stage and reach the line at p1. This information is stored in the working memory. For the duration of this calculated time, the particle is allowed to evolve in the transverse (x and y) directions only under the influence of the forces on the plane through p1 (perpendicular to the beam axis). The particle is then allowed to fly in the simulation cell until the ON time is reached, at which point the particle is stopped and the program records various parameters like position and speed. After relocating the particle back to the p1 line, the particle's trajectory is calculated using constant speed for the duration of OFF time period. At this point the particle's trajectory has undergone one full time-period evolution, passing through one stage of the device. The process is then repeated for as many stages as necessary.

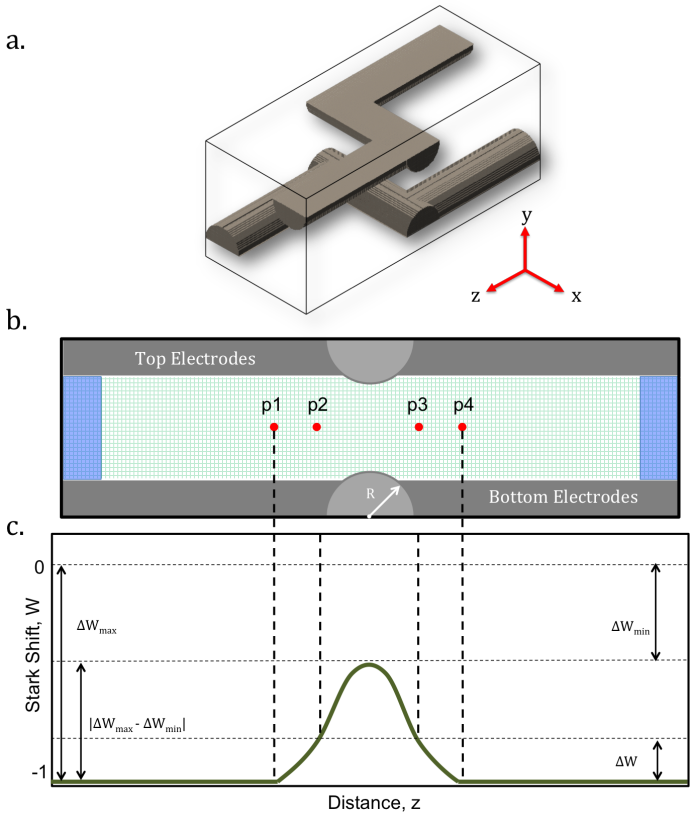

Figure 28. Example Simulation Cell for CoMP2. (a) An example of a three-dimensional simulation cell containing z-shaped electrodes (b) $z - y$ slice along the middle of the cell and (c) the corresponding Stark potential function.

In this scheme of utilizing the simulation cell a special attention must be paid to the cell boundaries (blue regions in Figure 28b). Particles that are moving too fast during ON time may exit the simulation cell resulting in particle termination.

As in CoMP1, it is also possible to use two (or more) PAs to simulate two (or more) field configurations by teleporting the particles from one PA into the other. Some of the easier electrode geometries, however, such as the z-shaped electrodes, make it possible to simulate an alternating gradient scenario without using multiple PAs but instead utilizing rotational symmetries of the resultant electric field.

4.5 Possible Experimental Setup

Our planned molecular beamline setup is shown in Figure 29. We prepare a beam of molecules by subjecting them to a seeded supersonic expansion with a noble gas or through buffer gas cooling as discussed in Section 4.1 and Section 4.1. In the case of the supersonic expansion, the emerging molecules have supersonic speeds in the lab frame but are cold in a frame that moves with the packet of molecules. In addition, a large portion of the molecules is in the ground electronic, rotational and vibrational state. One or two skimmers can be used to filter this plume of gas before it enters the microchip. After traversing the chip, molecules fly through a rectangular slit in a grounded shield. Past the shield, molecules encounter a microwave/mm-wave beam and a laser beam that, together, ionize the neutral molecule. By applying high voltage to the ion extraction plates we can remove the ionized molecules and slam them against the multichannel plate (MCP) detector that is coupled to a phosphor plate. The resulting light is detected by the charge-coupled device (CCD) camera connected to a computer.

In particular, as the molecules exit the decelerator chip they enter a laser beam and a millimeter wave (or microwave) beam, oriented 90 degrees to each other. The molecular beam passes through the rectangular slit of the shield prior to entering the area between the parallel ion-extraction plates where the beam is ionized. Grounding the shield is necessary to protect the chip from the electric field interference due to the ion extractor plates. The ionization is attained using the laser beam by way of species-selective resonance enhanced multiphoton ionization (REMPI) method while the characterization of the velocity and temperature spreads is accomplished using mm-wave (microwave) beam via measurement of the Doppler shift.

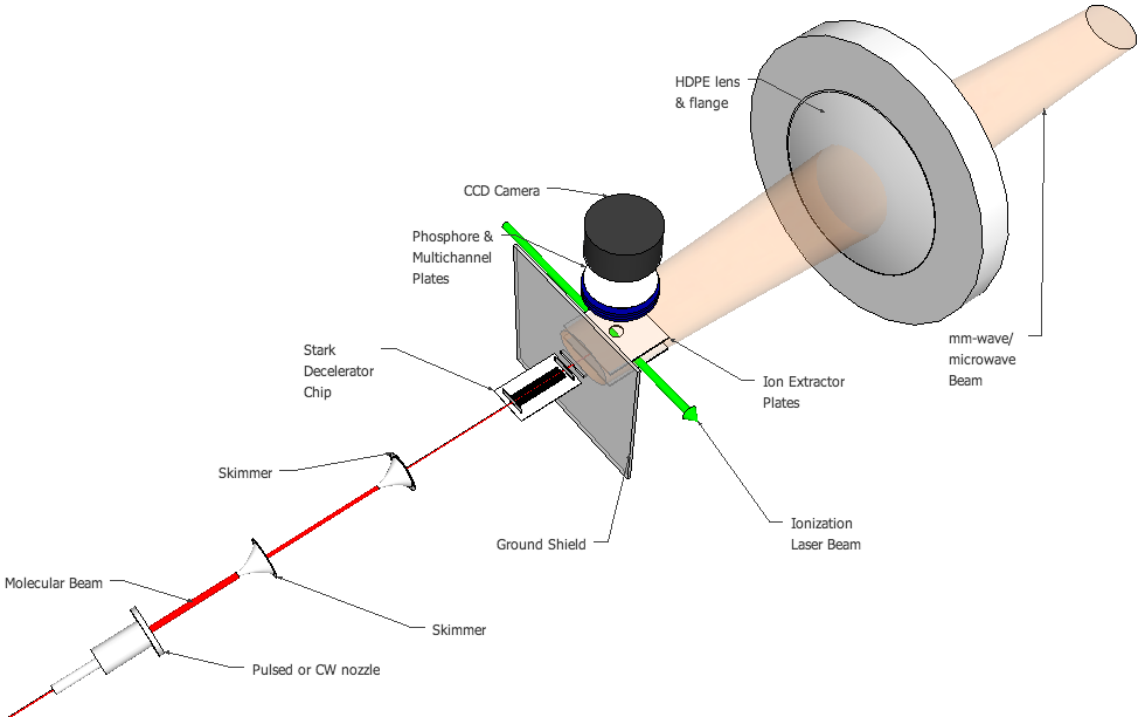

Figure 29. Possible Experimental Setup to Assess Microchip Performance. The components are contained in two differentially pumped high vacuum chambers. A beam of molecules (pulsed or CW) is emitted from the nozzle and passes through a skimmer or two before being manipulated by the microchip. Upon exiting, molecules are ionized and imaged by the CCD camera.

REMPI is one of the three most common laser ionization methods, the other two being the one-photon ionization (PI) and multiphoton ionization (MPI). However, PI and MPI are non-state-selective methods, whereas REMPI is state-selective and, in that sense, is much closer to laser-induced fluorescence (LIF). Typically, in the (n+m) REMPI process a molecule is excited to a resonant intermediate state (bound excited electronic state) after absorption of n photons (of energy h) followed by m photon promotion to the ionization continuum. The n and m photon transitions can be either of different or of the same frequency.

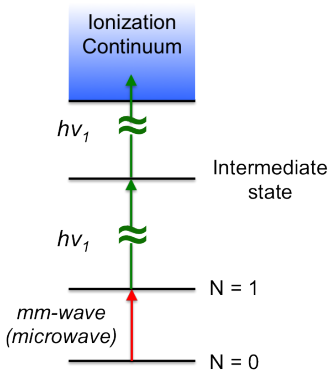

Figure 30. $(2+1)$ REMPI with Doppler Shift Measurement. The initial mm-wave (or microwave) beam is used to excite the molecule from the rotational ground state, $N = 0$, to the first excited state, $N = 1$. Then 2 photons are used to promote the molecule to an intermediate state with subsequent single photon ionization.

Some researchers, in fact, use two different lasers one to excite the molecule and the second laser to ionize it. Not all molecules can be ionized by REMPI. As with the LIF method the excited, intermediate state must have a sufficiently long lifetime for REMPI to work properly and this, in turn, requires one to know the ground and intermediate state spectroscopy for the molecule of interest (which is not always available). The benefit, however, is the ability to select molecules with a very specific quantum state without ionizing any other species present and the fact that ions can be collected and detected with nearly 100% efficiency (compared to LIF's fractional collection of photons and lower detector efficiencies of around 20%) [85].

In our set-up we plan to combine the REMPI process with the Doppler shift measurements using the mm-wave (microwave) beam, see Figure 30. In particular, the microwave/mm-wave beam excites the electronic and rotational ground-state ($N = 0$) molecule to the next rotational level ($N = 1$).

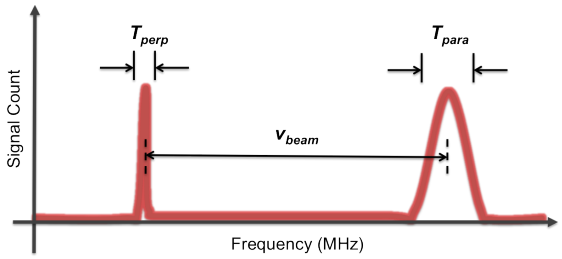

Figure 31. An Illustration of Doppler Profiles for mm-wave/Microwave Absorption.

We then use narrow bandwidth, high-energy, tunable pulsed dye laser (ND6000) that is pumped by a Nd:YAG laser in order to further promote the molecule to the intermediate state via virtual state (dashed line) using, for example, two photon absorption followed by a single photon ionization. The result is a molecular ion that, by applying voltage to the ion extraction plates, is extracted from the beam and accelerated towards the MCP detector. Eventually the ions slam against the MCPs initiating an electron avalanche process that excites the phosphor and the light produced is, in turn, detected by the CCD camera. Using REMPI with MCP+CCD detection scheme enables space resolved detection of the state-selective molecules.

Using this microwave/mm-wave scheme in combination with REMPI will enable us to determine the speed of the molecular beam and the temperature spreads (parallel and perpendicular) with the Doppler shift measurements. As an illustration, the Doppler profiles for mm-wave/microwave absorption is shown in Figure 31. Typically, one can record such profiles by either intersecting a single radiation beam with the molecular beam at 90° and at some other angle θ (by reflecting off of a mirror) or by intersecting the molecular beam at 90°, obtaining one peak, then positioning the source at some other angle θ, obtaining the second peak; if plotted on the same graph, the overlap of the two peaks would then produce the Doppler profiles shown.

In either case, all the relevant information about the molecular beam may be extracted from the Doppler profiles. The widths in the profiles stem from the distribution of energies that an ensemble of molecules absorbs as a result of the distribution of molecular speeds in the beam. Hence, knowing the widths enables us to calculate the temperatures of the beam from the full width at half maximum (FWHM) of the absorption Gaussian:

$$FWHM = v_0\sqrt{\frac{8ln(2)RT}{mc^2}} \tag{4.17}$$

where R is the gas constant, m is the mass of the molecule, c is the speed of light in a vacuum and T is the temperature (perpendicular or parallel) of the beam. The shift in the absorption energy due to a molecule traveling toward the mm-wave/microwave beam is:

$$v - v_0 = v_0\left(\frac{v_{beam}}{v_{phase}}\right)cos(\theta) \tag{4.18}$$

where v_0 and v are the frequencies seen by the molecule at rest and one traveling with speed v_{beam}. v_{phase} is the phase velocity of the radiation that for our purposes is equal to the speed of light c, and θ is the angle that the radiation beam makes with the molecular beam.

CHAPTER V

SUMMARY AND OUTLOOK

In this thesis a novel design of a Stark microchip able to control the motion of polar molecules with inhomogeneous electric fields is described. The architecture of the microchip, that is, the positioning of the stage electrodes and the corresponding electric field pulse sequence, is not simply a miniaturized version of the typical Stark decelerator. Instead, it is based on an alternative type of a decelerator, so-called *type-B*, in which the distance between the field-stages changes along the beam axis such that the device can be driven with a very simple voltage pulse sequence. Although the alternative architecture has been known since 2004, as of yet no device based on this architecture has been built or simulated. We propose that this alternative type may be best realized on a micro- rather than macroscale due to the significant improvements in positioning and alignment of the electrodes made possible by modern micro- and nanofabrication techniques. Unlike the typical macroscale Stark decelerators that can only decelerate one packet of molecules at a time, our device is capable of decelerating or accelerating multiple packets, thereby resulting in a (quasi) continuous beam of HFS/LFS polar molecules. This aspect is particularly attractive for trap loading and unloading since it can increase the overall operational frequency. The design is also flexible enough that it can readily be scaled having larger electrodes and separation distances. In such case, higher voltages ($> \pm 20$V) would have to be applied in order to achieve the same electric field gradients. Unlike typical Stark decelerators that must utilize complicated circuitry to produce the required voltage pulse sequence,

the applied voltage pulse sequence in our design is a constant-frequency pulse that can be easily adjusted with LC-type circuit (resonant circuit).

For an accelerator or decelerator to work efficiently a subset of particles, constituting the beam, must traverse the device in a stable manner. The principle of phase stability, discovered independently by V. Veksler [86] and E. McMillan [87] guarantees a constructive interaction between the particles and the electromagnetic fields that results in a net acceleration or deceleration. Constructive interaction here refers not only to the net effect of deceleration or acceleration, but also to the sustained grouping of the particles with diverse kinetic energies and positions. The results of the 1D simulation study, presented in Chapter II, confirm that the proposed design is capable of decelerating and accelerating polar molecules while maintaining phase stability. These results however, do not reveal the whole picture as they ignore transverse forces and any coupling that may occur between transverse and longitudinal motion. In order to also account for transverse forces a proper 3D simulation should be performed. The electrode geometry of the microchip design presented in Chapter II is (effectively) two-dimensional with gradients along longitudinal and only one transverse direction. This type of electrode geometry makes it practically impossible to implement a transverse focusing scheme such as alternating-gradient (AG) focusing. It may, nonetheless, be possible to achieve transverse focusing in such geometries using an alternating-phase focusing (APF) scheme proposed in Chapter III. We showed that the APF-like scheme can result in longitudinal stability but further simulation studies need to be done to confirm the feasibility of this scheme for transverse focusing as well.

At the expense of increasing the difficulty of the microchip fabrication, a transverse and longitudinal stability can be achieved using the AG scheme. In Chapter III, two different types of electrode geometries are presented that utilize AG focusing. The z-shape geometry relies on the particle's forward speed to alternate the gradients. On the other hand, the RFQ-type geometry alternates the transverse gradients by switching between two voltage configurations. This type of geometry has an additional degree of freedom, as far as transverse focusing is concerned, since the frequency of alternation can be arbitrarily specified. In both cases, the transverse motion can be stable only for certain switching frequencies (duty cycles) and can be described by the Mathieu-Hill type equations. Therefore, stability diagrams (a-q-maps) should be created to determine stable operation conditions.

REFERENCES

[1] F.-Q. Xie, L. Nittler, Ch. Obermair, and Th. Schimmel. Gate-Controlled Atomic Quantum Switch. *Physical Review Letters*, 93(12):128303, September 2004.

[2] Martin Fuechsle, Jill A Miwa, Suddhasatta Mahapatra, Hoon Ryu, Sunhee Lee, Oliver Warschkow, Lloyd C L Hollenberg, Gerhard Klimeck, and Michelle Y Simmons. A single-atom transistor. *Nature nanotechnology*, 7(4):242–6, April 2012.

[3] David P. DiVincenzo. The Physical Implementation of Quantum Computation. *Fortschritte der Physik*, 48(9-11):771–783, September 2000.

[4] A. Imamoglu, D. D. Awschalom, G. Burkard, D. P. DiVincenzo, D. Loss, M. Sherwin, and A. Small. Quantum Information Processing Using Quantum Dot Spins and Cavity QED. *Physical Review Letters*, 83(20):4204–4207, November 1999.

[5] L. Fedichkin, M. Yanchenko, and K. A. Valiev. Novel coherent quantum bit using spatial quantization levels in semiconductor quantum dot. page 16, June 2000.

[6] A. P. Nizovtsev. A Quantum Computer Based on NV Centers in Diamond: Optically Detected Nutations of Single Electron and Nuclear Spins. *Optics and Spectroscopy*, 99(2):233, 2005.

[7] William M. Kaminsky, Seth Lloyd, and Terry P. Orlando. Scalable Superconducting Architecture for Adiabatic Quantum Computation. page 5, March 2004.

[8] John Clarke and Frank K Wilhelm. Superconducting quantum bits. *Nature*, 453(7198):1031–42, June 2008.

[9] J. Preskill. Reliable quantum computers. *Proceedings of the Royal Society A: Mathematical, Physical and Engineering Sciences*, 454(1969):385–410, January 1998.

[10] T D Ladd, F Jelezko, R Laflamme, Y Nakamura, C Monroe, and J L O'Brien. Quantum computers. *Nature*, 464(7285):45–53, March 2010.

[11] D. J. Wineland, C. Monroe, W. M. Itano, D. Leibfried, B. E. King, D. M. Meekhof, and D. M. Meekhof D.J. Wineland, C. Monroe, W. M. Itano, D.

Leibfried, B. E. King. Experimental Issues in Coherent Quantum-State Manipulation of Trapped Atomic Ions. *J.Res.Natl.Inst.Stand.Tech.*, 103, October 1998.

[12] Rainer Blatt and David Wineland. Entangled states of trapped atomic ions. *Nature*, 453(7198):1008–15, June 2008.

[13] Marco Anderlini, Patricia J Lee, Benjamin L Brown, Jennifer Sebby-Strabley, William D Phillips, and J V Porto. Controlled exchange interaction between pairs of neutral atoms in an optical lattice. *Nature*, 448(7152):452–6, July 2007.

[14] Alpha Gaëtan, Yevhen Miroshnychenko, Tatjana Wilk, Amodsen Chotia, Matthieu Viteau, Daniel Comparat, Pierre Pillet, Antoine Browaeys, and Philippe Grangier. Observation of collective excitation of two individual atoms in the Rydberg blockade regime. *Nature Physics*, 5(2):115–118, January 2009.

[15] A. André, D. DeMille, J. M. Doyle, M. D. Lukin, S. E. Maxwell, P. Rabl, R. J. Schoelkopf, and P. Zoller. A coherent all-electrical interface between polar molecules and mesoscopic superconducting resonators. *Nature Physics*, 2(9):636–642, August 2006.

[16] Lincoln D. Carr, David DeMille, Roman V. Krems, and Jun Ye. Cold and ultracold molecules: Science, technology and applications. *New Journal of Physics*, 11, 2009.

[17] D DeMille. Quantum computation with trapped polar molecules. *Physical review letters*, 88(6):067901, 2002.

[18] Roman V. Krems, William Stwalley, and Bretislav Friedrich, editors. *Cold Molecules: Theory, Experiment, Applications*. CRC Press, 2009.

[19] Bretislav Friedrich and John M Doyle. Why are cold molecules so hot? *Chemphyschem : a European journal of chemical physics and physical chemistry*, 10(4):604–23, March 2009.

[20] Qi Wei, Sabre Kais, Bretislav Friedrich, and Dudley Herschbach. Entanglement of polar molecules in pendular states. *Journal of Chemical Physics*, 134(12):1–13, 2011.

[21] Andreas Osterwalder, Samuel a. Meek, Georg Hammer, Henrik Haak, and Gerard Meijer. Deceleration of neutral molecules in macroscopic traveling traps. *Physical Review A - Atomic, Molecular, and Optical Physics*, 81(5):1–5, 2010.

[22] Hendrick Bethlem. Electrostatic trapping of ammonia molecules. *Nature*, 406(6795), 2000.

[23] J. J. Gilijamse, S. Hoekstra, N. Vanhaecke, S. Y T Van De Meerakker, and G. Meijer. Loading Stark-decelerated molecules into electrostatic quadrupole traps. *European Physical Journal D*, 57(1):33–41, 2010.

[24] Samuel a. Meek, Horst Conrad, and Gerard Meijer. A stark decelerator on a chip. *New Journal of Physics*, 11:1–28, 2009.

[25] B G U Englert, M Zeppenfeld, M Mielenz, C Sommer, J Bayerl, M Motsch, P W H Pinkse, and G Rempe. Electric Trapping of Polar Molecules in a Microstructured Trap. 1:2–5.

[26] Y. Xia, L. Deng, and J. Yin. Electrostatic guiding of cold polar molecules on a chip. *Applied Physics B*, 81(4):459–464, July 2005.

[27] Qin Wang, Sheng-Qiang Li, Shun-Yong Hou, Yong Xia, Hai-Ling Wang, and Jian-Ping Yin. Electrostatic surface trap for cold polar molecules on a chip. *Chinese Physics B*, 23(1):013701, January 2014.

[28] Samuel A. Meek, Hendrick L. Bethlem, Horst Conrad, and Gerard Meijer. Trapping Molecules on a Chip in Traveling Potential Wells. *Physical Review Letters*, 100(15):153003, April 2008.

[29] Gabriele Santambrogio, Samuel A Meek, Mark J Abel, Liam M Duffy, and Gerard Meijer. Driving rotational transitions in molecules on a chip. *Chemphyschem : a European journal of chemical physics and physical chemistry*, 12(10):1799–807, July 2011.

[30] William H. Wing. On neutral particle trapping in quasistatic electromagnetic fields. *Progress in Quantum Electronics*, 8(3-4):181–199, 1984.

[31] Jacqueline Van Veldhoven, Hendrick L. Bethlem, and Gerard Meijer. Ac electric trap for ground-state molecules. *Physical Review Letters*, 94(8):1–4, 2005.

[32] Sophie Schlunk, Adela Marian, Wieland Schöllkopf, and Gerard Meijer. Ac electric trapping of neutral atoms. *Physical Review A - Atomic, Molecular, and Optical Physics*, 77(4):1–10, 2008.

[33] S. K Sekatskii and J Schmiedmayer. Trapping polar molecules with a charged wire. *Europhysics Letters (EPL)*, 36(6):407–412, November 1996.

[34] Melanie Schnell, Peter Lützow, Jacqueline Van Veldhoven, Hendrick L. Bethlem, Jochen Küpper, Bretislav Friedrich, Monika Schleier-Smith, Henrik Haak, and Gerard Meijer. A linear AC trap for polar molecules in their ground state. *Journal of Physical Chemistry A*, 111(31):7411–7419, 2007.

[35] Hendrick L. Bethlem, Jacqueline Van Veldhoven, Melanie Schnell, and Gerard Meijer. Trapping polar molecules in an ac trap. *Physical Review A - Atomic, Molecular, and Optical Physics*, 74(6):1–15, 2006.

[36] R. Blümel. Electrodynamic trap for neutral polar particles. *Physical Review A - Atomic, Molecular, and Optical Physics*, 83(4):2–4, 2011.

[37] T. Rieger, P. Windpassinger, S. a. Rangwala, G. Rempe, and P. W H Pinkse. Trapping of neutral rubidium with a macroscopic three-phase electric trap. *Physical Review Letters*, 99(6):1–4, 2007.

[38] Makoto Morinaga and Tetsuo Kishimoto. Planar electric trap for neutral particles. *Japanese Journal of Applied Physics*, 48(9 Part 1):0965051–0965056, 2009.

[39] R Blümel. Nano trap for polar molecules. *Journal of Physics B: Atomic, Molecular and Optical Physics*, 45(14):145301, 2012.

[40] Etay Lavert-Ofir, Sasha Gersten, Alon B. Henson, Itamar Shani, Liron David, Julia Narevicius, and Edvardas Narevicius. A moving magnetic trap decelerator: A new source of cold atoms and molecules. *New Journal of Physics*, 13:1–10, 2011.

[41] J. Riedel, S. Hoekstra, W. Jäger, J. J. Gilijamse, S. Y T Van De Meerakker, and G. Meijer. Accumulation of Stark-decelerated NH molecules in a magnetic trap. *European Physical Journal D*, 65(1-2):161–166, 2011.

[42] A. Trimeche, M. N. Bera, J. P. Cromières, J. Robert, and N. Vanhaecke. Trapping of a supersonic beam in a traveling magnetic wave. *European Physical Journal D*, 65(1-2):263–271, 2011.

[43] D. DeMille, D. R. Glenn, and J. Petricka. Microwave traps for cold polar molecules. *The European Physical Journal D*, 31(2):375–384, November 2004.

[44] R. Fulton, A. I. Bishop, M. N. Shneider, and P. F. Barker. Controlling the motion of cold molecules with deep periodic optical potentials. *Nature Physics*, 2(7):465–468, June 2006.

[45] Hendrick Bethlem, Giel Berden, and Gerard Meijer. Decelerating Neutral Dipolar Molecules. *Physical Review Letters*, 83(8):1558–1561, 1999.

[46] Hendrick L Bethlem, André J a van Roij, Rienk T Jongma, and Gerard Meijer. Alternate gradient focusing and deceleration of a molecular beam. *Physical review letters*, 88(13):133003, 2002.

[47] M. R. Tarbutt, H. L. Bethlem, J. J. Hudson, V. L. Ryabov, V. a. Ryzhov, B. E. Sauer, G. Meijer, and E. a. Hinds. Slowing heavy, ground-state molecules using an alternating gradient decelerator. *Physical Review Letters*, 92(17):173002–1, 2004.

[48] Sebastiaan Yt van de Meerakker, Hendrick L. Bethlem, Nicolas Vanhaecke, and Gerard Meijer. Manipulation and control of molecular beams. *Chemical Reviews*, 112(9):4828–4878, 2012.

[49] Samuel A. Meek. *A Stark decelerator on a chip*. PhD thesis, October 2010.

[50] E. a. Peralta, K. Soong, R. J. England, E. R. Colby, Z. Wu, B. Montazeri, C. McGuinness, J. McNeur, K. J. Leedle, D. Walz, E. B. Sozer, B. Cowan, B. Schwartz, G. Travish, and R. L. Byer. Demonstration of electron acceleration in a laser-driven dielectric microstructure. *Nature*, 503(V):91–94, November 2013.

[51] B. Friedrich. A quasi-analytic model of a linear Stark accelerator/decelerator for polar molecules. *European Physical Journal D*, 31(2):313–336, 2004.

[52] Stephan Putzke. *Alternating-gradient focusing of large neutral molecules*. PhD thesis, Fritz-Haber-Institut der Max-Planck-Gesellschaft, 2012.

[53] G Tomasevich. *Thesis*. PhD thesis, 1970.

[54] Hendrick L Bethlem, M R Tarbutt, Jochen Küpper, David Carty, Kirstin Wohlfart, E A Hinds, and Gerard Meijer. Alternating gradient focusing and deceleration of polar molecules. *Journal of Physics B: Atomic, Molecular and Optical Physics*, 39(16):R263–R291, August 2006.

[55] Hendrick L. Bethlem, Floris M. H. Crompvoets, Rienk T. Jongma, Sebastiaan Y. T. van de Meerakker, and Gerard Meijer. Deceleration and trapping of ammonia using time-varying electric fields. *Physical Review A*, 65(5):053416, May 2002.

[56] Koos Gubbels, Gerard Meijer, and Bretislav Friedrich. Analytic wave model of Stark deceleration dynamics. *Physical Review A - Atomic, Molecular, and Optical Physics*, 73(6):1–20, 2006.

[57] S Earnshaw. On the nature of the molecular forces which regulate the constitution of the luminiferous ether. *Trans. Camb. Phil. Soc*, 7:97 – 112, 1842.

[58] N. C Christofilos. Focusing System for Ions and Electrons, 1950.

[59] Daniel Auerbach. Alternate-Gradient Focusing of Molecular Beams. *The Journal of Chemical Physics*, 45(6):2160, 1966.

[60] M R Tarbutt and E A Hinds. Nonlinear dynamics in an alternating gradient guide for neutral particles. *New Journal of Physics*, 10(7):073011, July 2008.

[61] Alternating-gradient Synchrotron, E D Courant, and H S Snyder. Theory of the alternating-Gradient Synchrotron. 408:360–408, 1958.

[62] D. Kakati and D.C. Lainé. Alternate-gradient focusing of a molecular beam of ammonia. *Physics Letters A*, 24(12):676, June 1967.

[63] Wolfgang Paul. Electromagnetic traps for charged and neutral particles. *Reviews of Modern Physics*, 62(3):531–540, July 1990.

[64] Juris Kalnins, Glen Lambertson, and Harvey Gould. Improved alternating gradient transport and focusing of neutral molecules. *Review of Scientific Instruments*, 73(7):2557, 2002.

[65] J Reuss. State Selection by Nonoptical Methods. In Giacinto Scoles, editor, *Atomic and Molecular Beam Methods*, chapter 11, pages 284–289. Oxford University Press, 1988.

[66] Stephan Putzke, Frank Filsinger, Henrik Haak, Jochen Küpper, and Gerard Meijer. Rotational-state-specific guiding of large molecules. *Physical chemistry chemical physics : PCCP*, 13(42):18962–70, November 2011.

[67] Frank Filsinger, Undine Erlekam, Gert von Helden, Jochen Küpper, and Gerard Meijer. Selector for Structural Isomers of Neutral Molecules. *Physical Review Letters*, 100(13):133003, April 2008.

[68] T. E. Wall, S. Armitage, J. J. Hudson, B. E. Sauer, J. M. Dyne, E. A. Hinds, and M. R. Tarbutt. Transport of polar molecules by an alternating-gradient guide. *Physical Review A*, 80(4):043407, October 2009.

[69] I.M Kapchinsky and V.A Tepliakov. The Ion Linear Accelerator with Space-Uniform Strong Focusing. *Prib.Tech.Eksp*, 2:19, 1970.

[70] A.I Balabin. Numerical Calculations of the Acceleration and Focusing Effectiveness in RFQ Structures. Technical report, Institute of Theoretical and Experimental Physics, 1980.

[71] Louis A. Pipes. Matrix Solution of Equations of the Mathieu-Hill Type. *Journal of Applied Physics*, 24(7):902, June 1953.

[72] N V Konenkov, M Sudakov, and D J Douglas. Matrix methods for the calculation of stability diagrams in quadrupole mass spectrometry. *Journal of the American Society for Mass Spectrometry*, 13(6):597–613, June 2002.

[73] M. L Good. Phase-Reversal Focusing in Linear Accelerators. *Physical Review*, 92(2):538, 1953.

[74] Ya. B Faynberg. Alternating Phase Focusing in Linear Accelerators. *ZhTF*, 29(5):568, 1959.

[75] D.A. Swenson. Alternating phase focused linacs. *Particle Accelerators*, 7(2):61–67, 1976.

[76] B. P Murin. In *Proceedings of the 8th International Conference on High Energy Accelerators*, page 540, 1971.

[77] V. V Kushin. Increasing the Effectiveness of Alternating Phase Focusing in Linear Accelerators. *AE*, 29(2):123, 1970.

[78] B. P Murin, B. T Zarubin, S. V Zelentsov, V. S Kabanov, V. G Kul'man, V. V Kushin, and N. M Chistyakova. Proton Linear Accelerator with Alternating Phase Focusing. In *Proceedings of the 5th All-Union Conference on CPA*, page 330, 1978.

[79] J B Fenn. RESEARCH IN RETROSPECT:Some Biograffiti of a Journeyman Chemist. *Annual review of physical chemistry*, 47:1–41, January 1996.

[80] Nicholas R. Hutzler, Hsin I. Lu, and John M. Doyle. The buffer gas beam: An intense, cold, and slow source for atoms and molecules. *Chemical Reviews*, 112(9):4803–4827, 2012.

[81] David R. Miller. *Atomic and Molecular Beam Methods*, volume 1. 1988.

[82] Hendrick L. Bethlem, Giel Berden, Andre J a van Roij, Floris M H Crompvoets, and Gerard Meijer. Trapping neutral molecules in a traveling potential well. *Physical Review Letters*, 84(25):5744–5747, 2000.

[83] O. F. Hagena. Cluster Formation in Expanding Supersonic Jets: Effect of Pressure, Temperature, Nozzle Size, and Test Gas. *The Journal of Chemical Physics*, 56(5):1793, 1972.

[84] Hans Pauly. *Atom, Molecule, and Cluster Beams I.* Springer-Verlag Berlin Heidelberg, 1 edition, 200.

[85] Chapel Hill Tomas Baer Professor of Chemistry University of North Carolina and William L. Hase Department of Chemistry Wayne State University. *Unimolecular Reaction Dynamics : Theory and Experiments: Theory and Experiments*. Oxford University Press, USA, 1996.

[86] Vladimir Veksler. A New Method of the Acceleration of Relativistic Particles. *Doklady Akad. Nauk (USSR)*, 43(346), 1944.

[87] Edwin McMillan. The Synchrotron - A Proposed High Energy Particle Accelerator. *Physical Review*, 68(5-6):143–144, September 1945.